Cell Metabolism

Article

Liver-fibrosis-activated transcriptional networks govern hepatocyte reprogramming and intra-hepatic communication

Graphical abstract

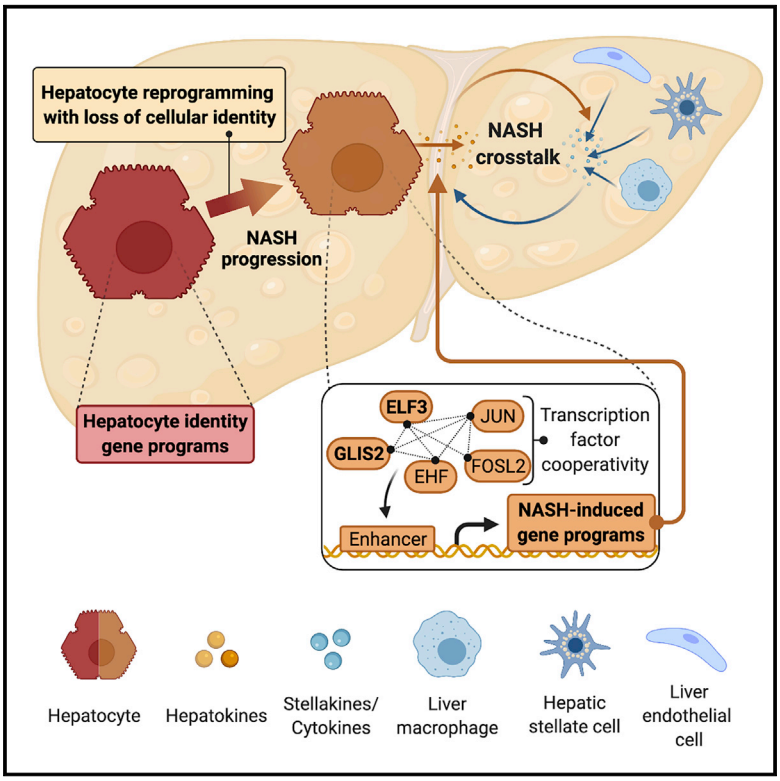

Highlights

- Advanced NASH is accompanied by partial loss of hepatocyte identity
- NASH-induced hepatokines associate with fibrosis-linked genes in hepatic stellate cells
- A cooperative transcription factor network drives hepatocyte genomic reprogramming in NASH
- Fibrosis-activated ELF3 and GLIS2 promote intra-hepatic crosstalk and liver fibrosis

Authors

Anne Loft, Ana Jimena Alfaro, Søren Fisker Schmidt, ..., Mauricio Berriel Diaz, Blagoy Blagoev, Stephan Herzig

Correspondence

anne.loft@helmholtz-muenchen.de (A.L.), stephan.herzig@helmholtz-muenchen.de (S.H.)

In brief

The mechanisms that drive the advanced stages of metabolic-associated fatty liver disease (MALFD) are still largely unknown. Using a cell type-resolved genomics approach, Loft et al. identified a fibrosis-activated hepatocyte transcription factor network that contributes to the loss of hepatocyte identity and dictates intra-hepatic cross-talk during the progression of MALFD.

Loft et al., 2021, Cell Metabolism *33*, 1–16
August 3, 2021
https://doi.org/10.1016/j.cmet.2021.06.005

CellPress

Cell Metabolism

CellPress

Article

Liver-fibrosis-activated transcriptional networks govern hepatocyte reprogramming and intra-hepatic communication

Anne Loft,[1,2,3,4,5,10,*] Ana Jimena Alfaro,[1,2,3,4,10] Søren Fisker Schmidt,[1,2,3,4,5] Felix Boel Pedersen,[5,6] Mike Krogh Terkelsen,[5,6] Michele Puglia,[5] Kan Kau Chow,[1,2,3,4] Annette Feuchtinger,[7] Maria Troullinaki,[1,2,3,4] Adriano Maida,[1,2,3,4] Gretchen Wolff,[1,2,3,4] Minako Sakurai,[1,2,3,4] Riccardo Berutti,[8] Bilgen Ekim Üstünel,[1,2,3,4] Peter Nawroth,[2,4,9] Kim Ravnskjaer,[5,6] Mauricio Berriel Diaz,[1,2,3,4] Blagoy Blagoev,[5,6] and Stephan Herzig[1,2,3,4,11,*]

[1]Institute for Diabetes and Cancer (IDC), Helmholtz Diabetes Center, Helmholtz Zentrum München, German Research Center for Environmental Health, Neuherberg 85764, Germany

[2]Joint Heidelberg-IDC Translational Diabetes Program, Heidelberg University Hospital, Heidelberg 69120, Germany

[3]Molecular Metabolic Control, Medical Faculty, Technical University Munich, München 80333, Germany

[4]German Center for Diabetes Research (DZD), Neuherberg 85764, Germany

[5]Department of Biochemistry and Molecular Biology, University of Southern Denmark, Odense 5230, Denmark

[6]Center for Functional Genomics and Tissue Plasticity (ATLAS), University of Southern Denmark, Odense 5230, Denmark

[7]Research Unit Analytical Pathology, Helmholtz Zentrum München, Neuherberg 85764, Germany

[8]Institute of Human Genetics, Helmholtz Zentrum München, Neuherberg 85764, Germany

[9]Department of Medicine I and Clinical Chemistry, Heidelberg University Hospital, Heidelberg 69120, Germany

[10]These authors contributed equally

[11]Lead contact

*Correspondence: anne.loft@helmholtz-muenchen.de (A.L.), stephan.herzig@helmholtz-muenchen.de (S.H.)

https://doi.org/10.1016/j.cmet.2021.06.005

SUMMARY

Liver fibrosis is a strong predictor of long-term mortality in individuals with metabolic-associated fatty liver disease; yet, the mechanisms underlying the progression from the comparatively benign fatty liver state to advanced non-alcoholic steatohepatitis (NASH) and liver fibrosis are incompletely understood. Using cell-type-resolved genomics, we show that comprehensive alterations in hepatocyte genomic and transcriptional settings during NASH progression, led to a loss of hepatocyte identity. The hepatocyte reprogramming was under tight cooperative control of a network of fibrosis-activated transcription factors, as exemplified by the transcription factor Elf-3 (ELF3) and zinc finger protein GLIS2 (GLIS2). Indeed, ELF3- and GLIS2-controlled fibrosis-dependent hepatokine genes targeting disease-associated hepatic stellate cell gene programs. Thus, interconnected transcription factor networks not only promoted hepatocyte dysfunction but also directed the intra-hepatic crosstalk necessary for NASH and fibrosis progression, implying that molecular "hub-centered" targeting strategies are superior to existing mono-target approaches as currently used in NASH therapy.

INTRODUCTION

The global prevalence of metabolic-associated fatty liver disease (MAFLD) is estimated to be around 25%, and a substantial number of individuals diagnosed with MAFLD further develop non-alcoholic steatohepatitis (NASH). In severe cases, NASH may progress to liver fibrosis, cirrhosis, and even hepatocellular carcinoma, with tremendous health and economic consequences (Younossi et al., 2018). In fact, liver fibrosis is the key predictor of long-term mortality in individuals diagnosed with MAFLD (Angulo et al., 2015), However, the mechanisms governing the transition from the fatty liver state to conditions of advanced NASH and liver fibrosis are not fully understood and no efficient NASH therapies are currently available (Friedman et al., 2018).

In a healthy liver, the hepatocytes constitute approximately 70% of all liver cells (Si-Tayeb et al., 2010) and non-parenchymal cells (NPC), including hepatic stellate cells (HSC), liver macrophages (LM), and liver endothelial cells (LEC) make up the rest. Besides accounting for most metabolic liver functions, such as gluconeogenesis as well as bile acid and complement factor synthesis, hepatocytes secrete a broad repertoire of signaling molecules, i.e., hepatokines that have been implicated in the regulation of systemic metabolism (Meex and Watt, 2017; Stefan and Häring, 2013). During the progression of NASH, stressed and dying hepatocytes promote recruitment of macrophages and activate HSC, mainly through the release of profibrogenic mediators, such as osteopontin (OPN) and hedgehog ligands, or through the release of profibrogenic damage-associated

Please cite this article in press as: Loft et al., Liver-fibrosis-activated transcriptional networks govern hepatocyte reprogramming and intra-hepatic communication, Cell Metabolism (2021), https://doi.org/10.1016/j.cmet.2021.06.005

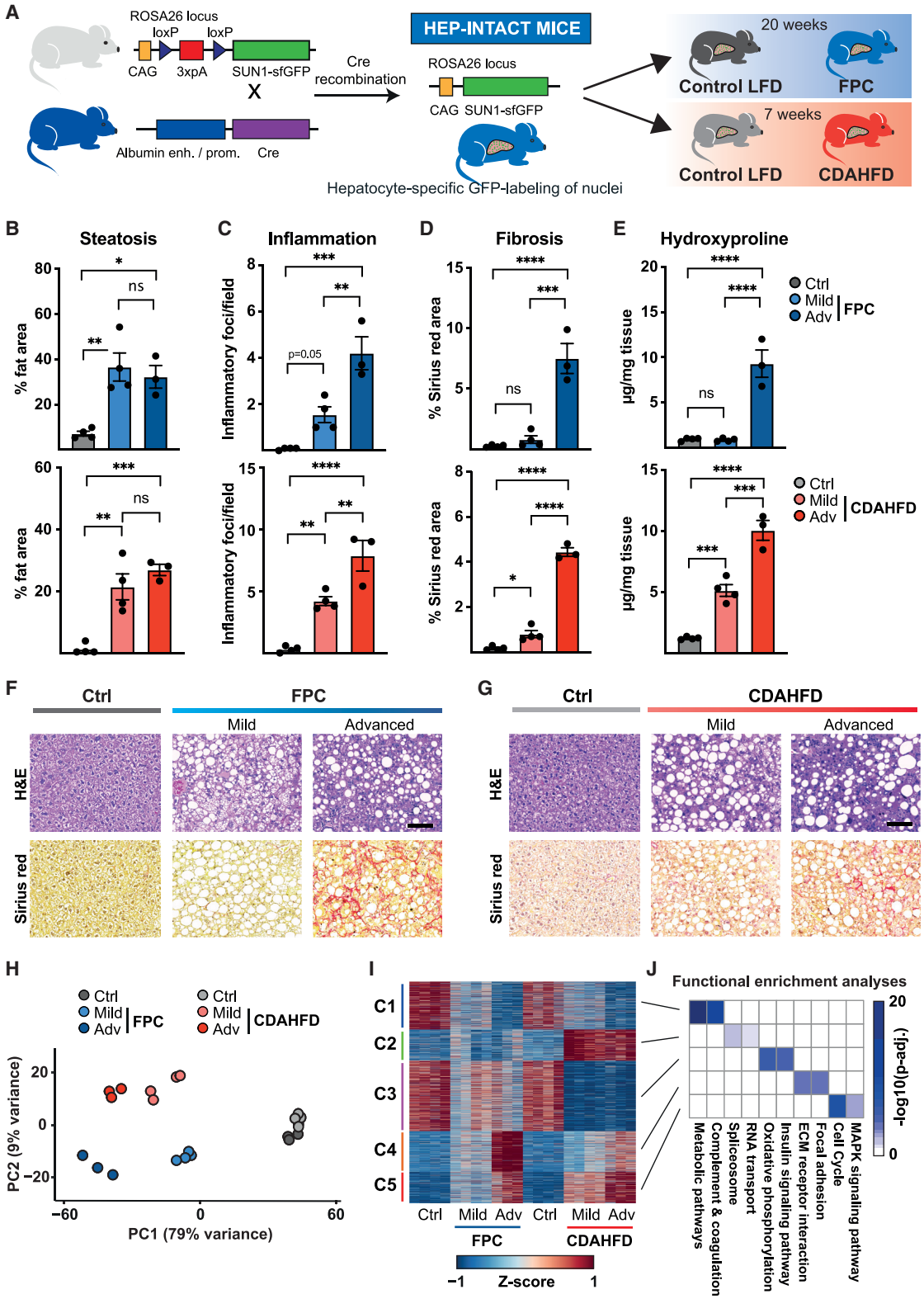

Figure 1. Hepatocyte-specific transcriptomics profiling in advanced NASH and liver fibrosis

HEP-INTACT mice were fed an FPC diet for 20 weeks or a CDAHFD for 7 weeks or the corresponding control diets

(A) Overview of the experimental approach.

(B) % liver fat area (n = 3–4).

(legend continued on next page)

Please cite this article in press as: Loft et al., Liver-fibrosis-activated transcriptional networks govern hepatocyte reprogramming and intra-hepatic communication, Cell Metabolism (2021), https://doi.org/10.1016/j.cmet.2021.06.005

molecular patterns (DAMPs) (Arriazu et al., 2017; Schwabe et al., 2020; Wang et al., 2016; Zhu et al., 2018). Yet, it is not fully understood how the hepatokine signature is altered in the advanced stages of NASH.

With the increased availability of NASH mouse models, the transcriptional mechanisms underlying NASH development are currently being unraveled. Several recent single-cell RNA-seq studies performed in mouse and human NASH livers have extensively characterized NPC populations and their intra-hepatic cross-talk in NASH and liver fibrosis (Dobie et al., 2019; Krenkel et al., 2020; Ramachandran et al., 2019, 2020; Seidman et al., 2020; Terkelsen et al., 2020; Xiong et al., 2019a). However, due to either poor recovery or depletion of the hepatocytes, much less has been learned about the role of hepatocytes from these studies (Ramachandran et al., 2020). Therefore, the mechanisms by which dysfunctional hepatocytes evolve in the more advanced stages of NASH and liver fibrosis are still largely unknown.

In recent years, integrative genomics approaches have facilitated the deciphering of the transcriptional mechanisms that control the development and specialized functions of multiple cell types from various tissues (Loft et al., 2017). In mouse livers, the chromatin accessibility is largely unaffected by high-fat feeding, and yet, there is still an activation of specific enhancers that are enriched for Cebp, Srebp, and Atf1/4 motifs, highlighting these factors as the most prominent transcriptional regulators of hepatic steatosis (Siersbæk et al., 2017). During the advanced stages of NASH and liver fibrosis, it is currently not known to what extent the hepatocyte enhancer landscape is altered and how it impacts on NASH manifestation.

Using a cell-type-resolved genomics approach, we characterized the genomic and transcriptional reprogramming specifically in hepatocytes as well as the hepatokine-mediated cross-talk during NASH progression. Our analyses revealed a fibrosis-activated hepatocyte transcription factor (TF) network, including ELF3 and GLIS2, that controls not only NASH-associated hepatocyte gene programs but also directs the intercellular communication with HSC and progression of NASH and liver fibrosis.

RESULTS

Hepatocyte-specific profiling reveals differential regulation of cancer signaling, cell-cycle, and metabolic pathways in advanced NASH

Based on the INTACT methodology (Deal and Henikoff, 2010; Mo et al., 2015), we generated HEP-INTACT (*Albumin-Cre; R26-CAG-LSL-Sun1-sfGFP-myc*) mice that allow cre-lox-driven cell-type-specific labeling and subsequent affinity purification of hepatocyte nuclei from intact liver tissues (Figure 1A). To explore the role of hepatocytes in the progression of NASH, we challenged HEP-INTACT mice with two different diets known to recapitulate key aspects of human NASH (Figure 1A). In one experiment, we fed mice a high-fat diet rich in fructose, palmitate, and cholesterol (i.e., the FPC diet) (Wang et al., 2016) or a control diet for 20 weeks. In a second experiment, we fed mice with a choline-deficient, methionine-reduced high-fat diet (CDAHFD) (Matsumoto et al., 2013) or a low-fat control diet for 7 weeks. The fraction of hepatocytes in the liver, as estimated by the fraction of GFP positive nuclei versus total liver nuclei in HEP-INTACT mice, became significantly lower with both diets demonstrating a significant change in the cellular composition during NASH progression (Figure S1A). This was further illustrated by RNA-seq and functional enrichment analyses of nuclei obtained from whole livers. In line with previous findings demonstrating that inflammatory pathways dominated the NASH-induced program (Ægidius et al., 2020; Xiong et al. 2019b), our data further emphasized the requirement for cell-type-specific approaches in experimental conditions that lead to changes in the cellular composition of the liver (Figure S1B).

It is well known that feeding mice with NASH-inducing diets leads to the acquisition of a heterogeneous liver disease phenotype that ranges from simple steatosis to more severe cases of steatohepatitis, fibrosis, and even cirrhosis (Clapper et al., 2013). We took advantage of the heterogeneous response and stratified the mice in each experiment into 3 groups based on the severity of the liver disease phenotype. The control group had been fed a low-fat-containing diet (Ctrl) and had low levels of liver fat and no signs of inflammation and fibrosis (Figures 1B–1G). The mice fed the NASH-inducing diets were divided into a mild NASH and an advanced NASH group with comparable higher levels of steatosis in the liver compared with the controls, whereas mice with advanced NASH had significantly more inflammatory foci and collagen fiber formation compared with mice with mild NASH (Figures 1B–1G). Several other physiological parameters differed between mice with mild and advanced NASH, including liver weight, serum albumin levels, and levels of liver damage markers in serum (Figures S1C and S1D; Table S1). In accordance with their more severe fibrosis status, the whole livers of mice with advanced NASH had higher expression of the fibrosis marker, *Col1a1*, and the inflammatory marker, *Tnf*, whereas other markers of LM and activated HSC did not change significantly in mice with mild and advanced NASH (Figures S1E and S1F).

(C) Number of inflammatory foci/fields in liver sections (n = 3–4).
(D) % Sirius red area in the liver (n = 3–4).
(E) Hydroxyproline content in the liver (n = 3–4).
(F and G) Representative hematoxylin and eosin (H&E) (upper) and Sirius red (lower) stainings of HEP-INTACT mice fed (F) an FPC diet or (G) a CDAHFD. Black bars indicate 100 μm.
(H) Principal component analyses of the RNA-seq data from GFP+ nuclei isolated from the HEP INTACT mice.
(I) K-means clustering of row-scaled $\log_2$ fold changes (log2FC) in expression of hepatocyte genes differentially expressed ($p_{adj} < 0.001$) between one or more conditions in GFP+ nuclei from HEP INTACT mice.
(J) Functional enrichment analyses using KEGG pathways for the indicated RNA-seq clusters.
(B–E and H) Every dot represents one individual mouse. (B–E) Colored bars indicate mean ± SEM. Significance was determined by one-way ANOVA with Tukey's multiple comparison test between the different conditions. *p < 0.05, **p < 0.01, ***p < 0.001, ****p < 0.0001, ns, non-significant.
See also Figure S1.

Please cite this article in press as: Loft et al., Liver-fibrosis-activated transcriptional networks govern hepatocyte reprogramming and intra-hepatic communication, Cell Metabolism (2021), https://doi.org/10.1016/j.cmet.2021.06.005

To monitor the transcriptional changes specifically in hepatocytes during the progression of NASH, we performed RNA-seq profiling of GFP+ nuclei isolated from the livers of control and diet-induced NASH mice. We confirmed that the expression of NPC marker genes was much lower across all conditions in GFP+ nuclei compared with whole liver nuclei, whereas hepatocyte marker gene expression was higher (Figure S1G). Principle component analyses (PCA) analyses of the RNA-seq data showed that GFP+ nuclei from the livers of control and diet-induced NASH mice, separated strongly in accordance with the liver health status in PC1 (Figure 1H). Furthermore, k-means clustering of genes that were differentially expressed in one or more of the experimental conditions revealed three clusters that were regulated specifically in mice with advanced NASH (i.e., clusters 1, 4, and 5) (Figures 1I and S1H). Pathway enrichment analyses demonstrated that genes induced specifically in the advanced NASH state belonged to the classes of cell matrix adhesions, as well as cell-cycle and cancer-related signaling pathways (Figure 1J). Genes repressed in advanced NASH were assigned to metabolic pathways and key liver processes (Figure 1J), overall demonstrating that hepatocytes react with a specific transcriptional response to NASH development.

Hepatocyte reprogramming during NASH progression is associated with loss of cellular identity

To understand the underlying transcriptional mechanisms driving the prominent changes in gene expression in hepatocytes during NASH progression, we performed ATAC-seq in GFP+ nuclei isolated from the livers of control and diet-induced NASH mice. Here, we identified almost 70,000 high-confidence accessible chromatin regions across all samples that were separated in accordance with the severity of the liver disease phenotype by PCA analyses (Figure S2A). We found that the hepatocyte chromatin landscape was highly dynamic during the progression of NASH in a manner that correlated between the two mouse models as well as with the pattern of nearby gene expression (Figures 2A–2C and S2B). Genomic regions that closed down in advanced NASH were often found near hepatocyte identity genes, e.g., encoding key hepatocyte metabolic enzymes, whereas *de novo* NASH-associated open regions formed in the vicinity of genes highly induced in NASH as illustrated in the *Glis2* locus (Figure 2B). We therefore asked if progression of NASH led to the loss of hepatocyte identity by examining so-called super-enhancers (SE), which are clusters of enhancers in close proximity known to control the expression of genes defining cell identity (Whyte et al., 2013). We used our ATAC-seq data to define SE regions in the control and advanced NASH conditions and found that the set of SE-associated identity genes changed between the control and advanced NASH conditions (Figure S2C). Furthermore, during NASH progression, hepatocyte genes associated with a SE in GFP+ control nuclei (i.e., hepatocyte identity genes) were repressed to a greater extent in advanced NASH than genes associated with a typical enhancer, indicating a specific effect on these hepatocyte identity genes during NASH progression (Figure S2D). Of note, this set of hepatocyte identity genes was highly enriched in the NASH-repressed hepatocyte RNA-seq cluster 1 and was associated with key hepatocyte metabolic pathways (Figures 2D and S2E). We confirmed this selective and prominent effect on a set of hepatocyte identity genes defined by the broad H3K4me3 domains encompassing the transcriptional start site in mouse livers (Dubois et al., 2020), which is another strong predictor of cell-identity genes (Benayoun et al., 2014) (Figure S2D). Interestingly, analyses of proteomics data revealed that proteins downregulated in mouse NASH livers (Xiong et al., 2019b) as well as in a human cohort of alcoholic-derived liver fibrosis (Niu et al., 2020) were highly enriched for proteins encoded by hepatocyte identity genes, highlighting the clinical relevance of identity loss in liver fibrosis (Figures 2E–2G).

Mutual cross-talk between hepatocytes and non-parenchymal cells during NASH progression

Next, we focused on understanding the intra-hepatic crosstalk between hepatocytes and other cell types during NASH progression by combining our hepatocyte RNA-seq dataset with single-cell RNA-seq data of NPCs obtained from healthy and fibrotic mouse livers (Terkelsen et al., 2020). First, we used NicheNet's computational intercellular communication analyses (Browaeys et al., 2020) to identify several fibrosis-induced NPC-derived ligands that had high potential for regulating the NASH-induced hepatocyte gene programs (i.e., focal adhesions, cancer-related signaling, and cell-cycle genes in RNA-seq clusters 4 and 5) (Figure 3A and 3B). Most significantly, transforming growth factor beta 1 (TGFB1) and high mobility group box 2 (HMGB2) had several predicted target genes in all of the major NASH-induced hepatocyte pathways acting via various hepatocyte target receptors (Figures 3C, S3A, and S3B).

To gain a comprehensive view of how NASH-induced hepatokines (in the following used to denote factors secreted from hepatocytes) could influence fibrosis-regulated gene programs in HSC, LM, and LEC (Table S2), we compiled a list of 37 putative hepatokines that were selectively induced in the advanced NASH state in both mouse models (Figure 3D). For 33 of these factors, NicheNet contained ligand-target gene interaction information, which was used to rank these ligands according to their potential to modulate NPC gene programs (Figure 3E). The most highly ranked NASH-induced hepatokines were predicted to have several prominent target genes, especially in HSC, acting via a broad range of target receptors on the NPCs (Figures 3F and S3C). Reassuringly, some of these hepatokines have previously been shown to be causal for NASH and liver fibrosis development, such as secreted phosphoprotein 1 (SPP1/OPN) and C-C motif chemokine 2 (CCL2) (Baeck et al., 2012; Zhu et al., 2018). Thus, our data supported and extended the observation that hepatokines play an active role in the development of liver fibrosis and predicted a hepatokine signature with a potential impact on disease-induced gene programs in NPCs.

Prediction of transcription factors driving NASH-induced reprogramming of hepatocytes

To dissect causal TFs responsible for the observed transcriptional changes in hepatocytes during NASH progression, we applied a machine learning approach that estimates the contribution of TF motifs to transcriptional activity (i.e., motif activity) (Madsen et al., 2018). In total, 64 motifs displayed differential motif activity ($p_{adj} < 0.01$) in one or both of the advanced NASH conditions (Figure 4A; Table S3). This included the master hepatocyte regulators, hepatocyte nuclear factor 4-alpha (HNF4A), hepatocyte nuclear

Please cite this article in press as: Loft et al., Liver-fibrosis-activated transcriptional networks govern hepatocyte reprogramming and intra-hepatic communication, Cell Metabolism (2021), https://doi.org/10.1016/j.cmet.2021.06.005

CellPress

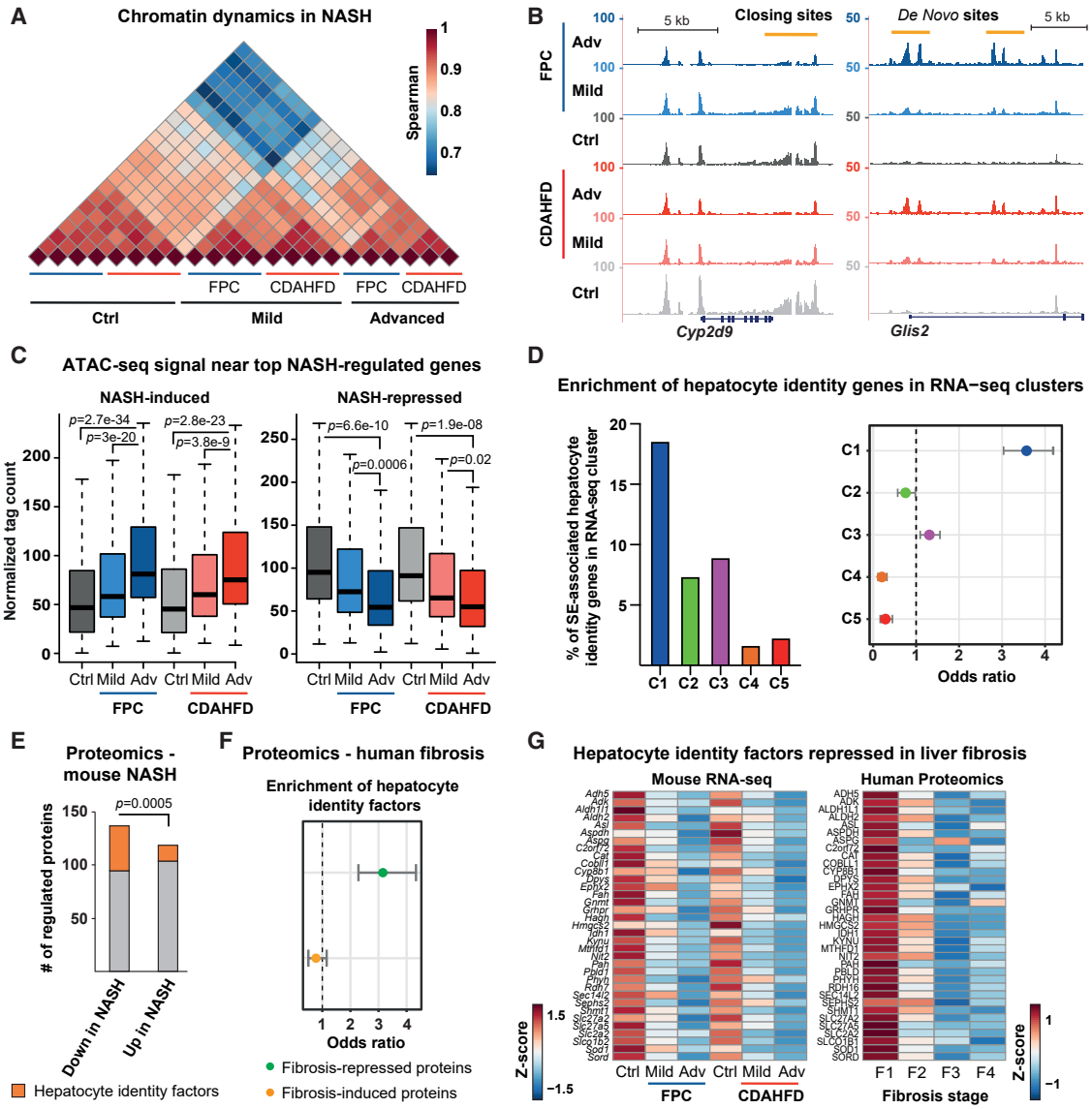

Figure 2. Progression of NASH leads to loss of hepatocyte identity

(A) Similarity heatmap showing Spearman correlation of normalized ATAC-seq tag counts (68,827 ATAC-seq sites) in GFP+ nuclei obtained from HEP INTACT mice fed control or NASH-inducing diets.

(B) UCSC genome browser screenshots showing ATAC-seq read density in the *Cyp2b9* (left) or *Glis2* (right) loci in GFP+ nuclei from HEP INTACT mice.

(C) Normalized ATAC-seq tag count in the vicinity of top NASH-induced ($log_2FC > 2$, left) or NASH-repressed ($log_2FC < -2$, right) genes in GFP+ nuclei from HEP INTACT mice.

(D) % of total number (left) and enrichment (as indicated by odds ratio) (right) of SE-associated hepatocyte identity genes identified in the control condition in each RNA-seq cluster.

(E) Bar plot showing the number of all regulated proteins as well as regulated proteins encoded by hepatocyte identity genes (orange) in mouse NASH versus control livers (Xiong et al., 2019b).

(F) Enrichment (as indicated by odds ratio) of hepatocyte identity genes encoding for proteins repressed (green) or induced (orange) in fibrotic livers of human individuals diagnosed with alcoholic steatohepatitis (ASH) (Niu et al., 2020).

(G) Heatmaps of the common set of fibrosis-repressed hepatocyte identity factors. Row-scaled mean expression of mouse genes in GFP+ nuclei from HEP INTACT mice (left) and row-scaled mean intensity of human proteins according to fibrosis stage (F0 to F4) in fibrotic livers of human individuals diagnosed with ASH (right).

(C) horizontal line indicates the median and whiskers indicate 1.5× IQR.

(D and F) The circle indicates odds ratio with 95% confidence interval. Significance was determined using (C) a two-sided Wilcoxon–Mann–Whitney test or (D–F) a Fisher's exact test and indicated by (C and E) exact p value or (D and F) the odds ratio.

See also Figure S2.

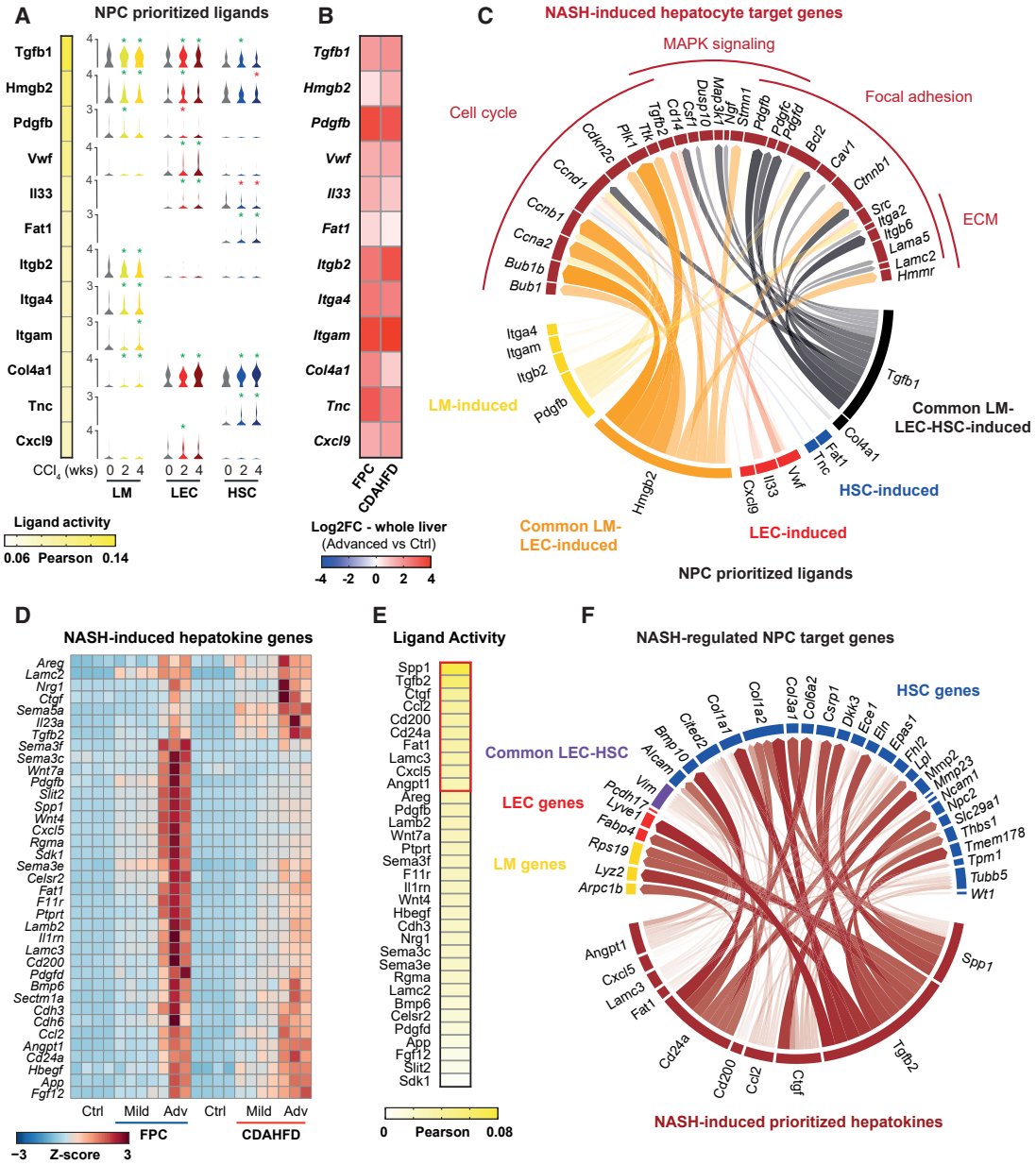

Figure 3. Mutual crosstalk between hepatocytes and non-parenchymal cells during NASH progression

(A) Ligand activity of top predicted upstream ligands from non-parenchymal cells (NPC) (left) and violin plots showing a scaled log_2-normalized expression (scRNA-seq) of selected genes in liver macrophages (LM), liver endothelial cells (LEC), and hepatic stellate cells (HSC) obtained from livers of control and carbon tetrachloride (CCl_4)-induced fibrotic mice (right).

(B) Log2FC in gene expression (RNA-seq) in whole liver nuclei from HEP-INTACT mice (advanced NASH versus control group) for indicated genes.

(C) Circle plot showing predicted interaction links between NASH-induced NPC ligands in LM (yellow), LEC (red), HSC (blue), common in LM and LEC (orange), or common in all NPC (black) to their associated NASH-induced putative hepatocyte target genes (bordeaux) associated with the indicated KEGG pathway. ECM, extra cellular matrix-receptor interaction.

(D) Heatmap showing row-scaled expression (RNA-seq) for NASH-induced genes encoding predicted hepatokines in GFP+ nuclei from HEP INTACT mice.

(E) NicheNet's ligand activity of predicted hepatokines.

(F) Circle plot showing the predicted interaction links between top NASH-induced hepatokines (bordeaux) to their associated NASH-induced genes regulated in LM (yellow), LEC (red), HSC (blue) or commonly in LEC and HSC (purple).

(A) Significance was determined by two-sided Wilcoxon–Mann–Whitney test. *p < 0.001 (green, induced and red, repressed).

See also Figure S3.

Please cite this article in press as: Loft et al., Liver-fibrosis-activated transcriptional networks govern hepatocyte reprogramming and intra-hepatic communication, Cell Metabolism (2021), https://doi.org/10.1016/j.cmet.2021.06.005

CellPress

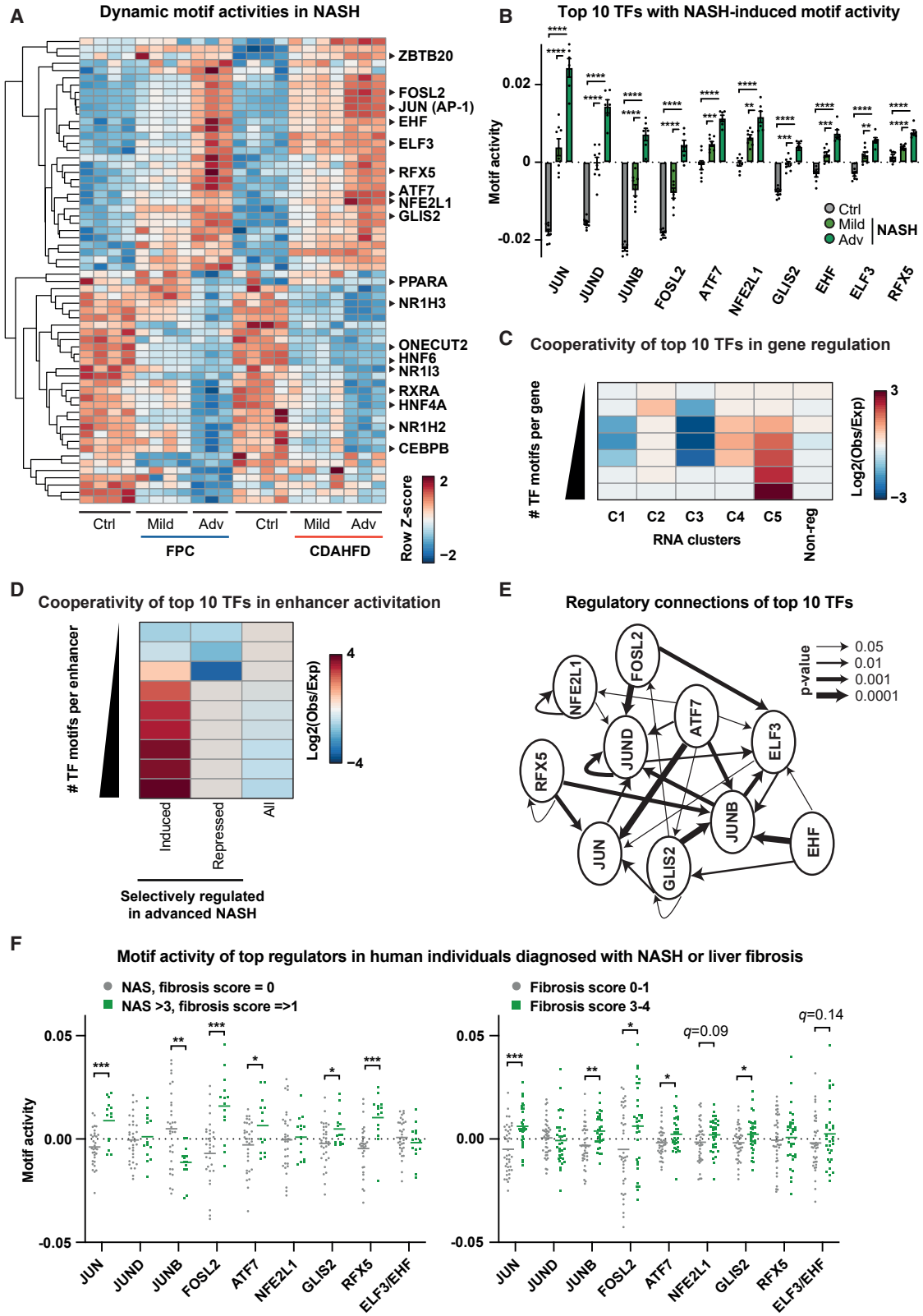

Figure 4. Transcription factor network driving NASH progression

(A) Heatmap showing 64 significantly altered (p_{adj} < 0.01) row-scaled and hierarchically clustered motif activities during NASH progression.

(B) Averaged motif activity (FPC and CDAHFD study) for top 10 predicted transcription factors (TF) with NASH-induced motif activities (n = 6–8)

(legend continued on next page)

factor 6 (HNF6/ONECUT1), and one cut domain family member 2 (ONECUT2), which all had reduced motif activity in advanced NASH (Figure S4A) consistent with the loss of hepatocyte identity. Next, we focused on the TFs that gained motif activity during NASH progression and selected for factors predicted to be particularly important in the transition from simple to the more severe stages of NASH and liver fibrosis. Some top predicted factors had been implicated in MAFLD or NASH before, such as members of the activator protein-1 (AP-1) family (Hasenfuss et al., 2014), but a number of new putative regulators were identified (Figure 4B). Some of these factors were also induced at the transcriptional level during NASH progression, whereas the activity of other factors may be activated predominantly at the post-transcriptional level (Figure S4B). Next, we predicted target sites of all top regulatory TFs *in silico* and, as a proof of principle, demonstrated that computationally predicted JUN target sites were most highly concordant with experimentally validated JUN binding sites obtained in mouse primary hepatocytes (Figure S4C). Several of the predicted target sites were shared between two or more of the TFs (Figures S4D and S4E) and these TFs seemed to act in a highly cooperative manner to activate both hepatocyte target enhancers as well as target genes selectively induced in advanced NASH (Figures 4C, 4D, and S4F, and S4G). Interestingly, these TFs appeared to be engaged in an interconnected regulatory network, since several TFs were predicted targets for themselves or of one or more of the other TFs in the network (Figure 4E). Furthermore, by combining our INTACT data and publicly available ChIP-seq data generated in a human hepatocellular carcinoma (HCC) cell line with binding and expression target analysis (BETA) (Wang et al., 2013), we demonstrated that the majority of the top predicted NASH-induced hepatokine genes were likely targets of one or more of the top regulatory TFs (Figure S4H and S4I). Finally, to explore the significance of the predicted regulators in humans, we mined public available microarray data using the integrated system for motif activity response analysis (ISMARA), which estimates motif activity in gene promoter-proximal regions (Balwierz et al., 2014). Intriguingly, several of the candidate TFs displayed either a significant or a trending higher motif activity in human individuals diagnosed with NASH or liver fibrosis compared with controls, supporting the notion that these regulators were also activated during progression of human NASH (Figures 4F and S4J).

Disease-activated ELF3 and GLIS2 regulate NASH progression

Since our analyses predicted several new potential regulators of hepatocyte reprogramming in advanced NASH, we selected two of these TFs for functional investigations, namely ELF3 and GLIS2. ELF3 is a member of the E26-transformation-specific TF family and has previously been implicated in the epithelial-mesenchymal transition (EMT) in HCC cell lines (Zheng et al., 2018). GLIS2 is a member of the GLI-similar zinc finger protein family and is known for its role in kidney disease development (Attanasio et al., 2007). During NASH progression, ELF3 and GLIS2 were, in addition to having higher motif activity, induced both at the transcriptional and protein level in our NASH models (Figure 5A and 5B). Accordingly, both *Elf3* and *Glis2* expression was also higher in the livers of several other NASH animal models compared in controls and also generally trended toward being induced in human NASH (Figure 5C). Of note, both *Elf3* and *Glis2* were predicted target genes of other members of the regulatory NASH-activated TF network, which might be involved in coordinating their transcriptional induction during NASH progression (Figure 4E). The induction of *Elf3*, *Glis2* as well as a large subset of the NASH-activated gene program was likely occurring in a subpopulation of NASH-transformed hepatocytes, since the expression of the majority of these NASH-activated genes was induced in reprogrammed biliary-like hepatocytes following liver injury (Figures S5A and S5B) (Merrell et al., 2021). To investigate the impact of ELF3 and GLIS2 in the transition from mild to advanced NASH, we fed mice an FPC diet for 14 weeks, allowing them to develop a significant degree of steatosis with no evident signs of fibrosis (Figures 5D and S5C). Then, we used an adeno-associated virus (AAV)-miRNA delivery approach (Kulozik et al., 2011; Nathwani et al., 2006; Rose et al, 2011) to knock down (KD) *Elf3* or *Glis2* specifically in hepatocytes and continued the FPC diet feeding until 10 weeks post injection (Figures 5D and Figures S5D). For mice with *Elf3* or *Glis2* KD, we found a significant reduction in several parameters linked to advanced NASH and liver fibrosis, including apoptosis, inflammatory cell infiltration, and collagen fiber formation, whereas no effect on steatosis was observed (Figures 5E–5I and S5E–S5G; Table S4). Accordingly, the expression of NASH-induced fibrosis-, apoptosis- and inflammatory marker genes was reduced in the livers of mice with *Elf3* or *Glis2* KD (Figures 5J and S5H–S5J).

ELF3 and GLIS2 control NASH-activated gene programs in hepatocytes

The impact of ELF3 and GLIS2 loss-of-function on NASH phenotypes prompted us to next investigate the mechanism of ELF3 and GLIS2 action using RNA-seq analyses. FPC-induced genes that showed less induction by *Elf3* and/or *Glis2* KD (i.e., KD-repressed genes) belonged to cell-matrix-adhesion and

(C) Enrichment of RNA-seq clusters for TF target genes for an increasing number of TFs with NASH-induced motif activities. Enrichment is indicated in comparison to a random distribution (observed/expected).
(D) Enrichment of advanced NASH-regulated genomic regions for TF target sites for an increasing number of TFs with NASH-induced motif activities. Enrichment is indicated in comparison to a random distribution (observed/expected).
(E) Regulatory relationship of the NASH-activated TF network. The direction of the arrow indicates that the targeted factor is a predicted target gene of the connected factor and the width of lines indicates the significance level of the target gene prediction.
(F) Motif activity in two human cohorts of NASH and liver fibrosis for top 10 predicted TF with NASH-induced motif activities (n = 14–40)
(B and F) Every dot represents one individual (B) mouse or (F) human sample. Colored bars indicate (B) mean ± SEM or (F) horizontal-colored lines indicate mean. Significance was determined by (B) one-way ANOVA with Dunnett's multiple comparison test between motif activities for advanced NASH versus control or mild NASH for each motif or (F) multiple t test with FDR correction between motif activities for control individuals versus individuals diagnosed with NASH/liver fibrosis. $^{**}p < 0.01$, $^{***}p < 0.001$, $^{****}p < 0.0001$, or when corrected for multiple testing by $^{*}q < 0.05$, $^{**}q < 0.01$, $^{***}q < 0.001$.
See also Figure S4.

Please cite this article in press as: Loft et al., Liver-fibrosis-activated transcriptional networks govern hepatocyte reprogramming and intra-hepatic communication, Cell Metabolism (2021), https://doi.org/10.1016/j.cmet.2021.06.005

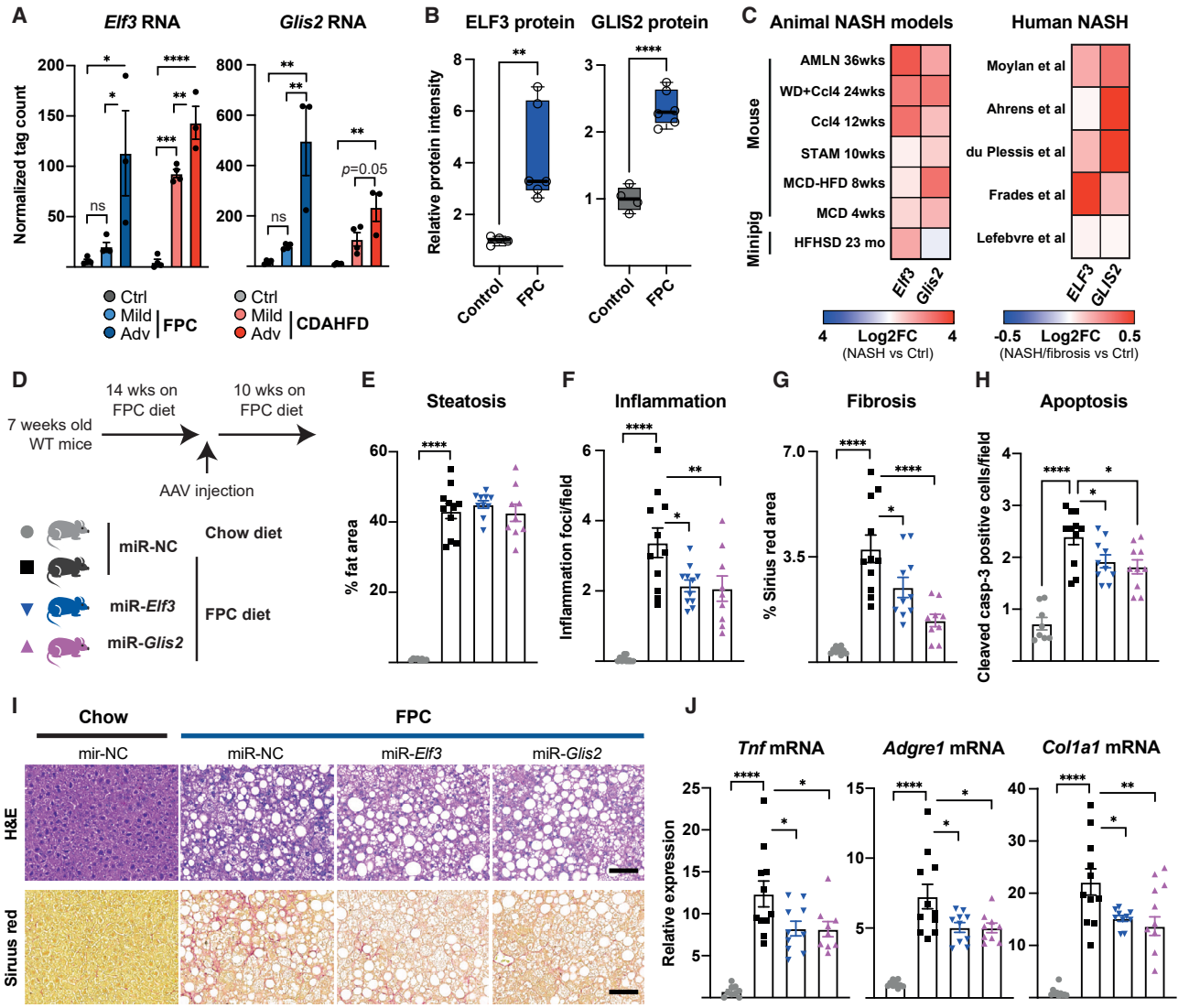

Figure 5. Disease-activated ELF3 and GLIS2 are regulators of advanced NASH

(A) Expression (RNA-seq) of *Elf3* and *Glis2* in GFP+ nuclei from HEP INTACT mice (n = 3–4)

(B) Relative protein levels (targeted nuclear proteomics) of ELF3 and GLIS2 in livers obtained from control and mice fed an FPC diet (n = 4–6).

(C) Log2FC in *Elf3* and *Glis2* expression (microarray or RNA-seq) in various mouse models and a minipig model of NASH (left) and in indicated human cohorts of NASH and liver fibrosis (right). (WD, western diet; AMLN, amylin liver NASH; CCl_4, carbon tetrachloride; MCD-HFD, methionine; choline-deficient high-fat diet; HFHSD, high-fat, high-sucrose diet)

(D) Mice were fed control or FPC diet for 14 weeks, injected with AAVs expressing non-coding miRNAs (miR-NC) or miRNA against *Elf3* (miR-*Elf3*) or *Glis2* (miR-*Glis2*) and kept on the diet for additional 10 weeks.

(E) % fat area in the liver (n = 9–11).

(F) Number of inflammatory foci/fields in liver sections (n = 9–11).

(G) % Sirius red area in the liver (n = 9–11).

(H) Number of cleaved caspase-3-positive cells/field in liver sections (n = 9–11).

(I) Representative H&E (upper) and Sirius red stainings (lower). Black bar indicates 100 μm.

(J) Expression (qPCR) of indicated genes in whole liver (n = 9–11).

(A, B, E–H, and J) Every dot/square/triangle represents one individual mouse. (A, E-H, J) Bars indicate mean ± SEM and (B) horizontal line indicates the median and whiskers indicate min-to-max. Significance was determined by (A) one-way ANOVA with Tukey's multiple comparison test between the conditions in each study, (B) two-sided, unpaired t test or (E–H, J) one-way ANOVA with post-hoc Dunnett's multiple comparison test between FPC-fed mice injected with miR-NC and the other conditions. *p < 0.05, **p < 0.01, ***p < 0.001, ****p < 0.0001.

See also Figure S5.

Please cite this article in press as: Loft et al., Liver-fibrosis-activated transcriptional networks govern hepatocyte reprogramming and intra-hepatic communication, Cell Metabolism (2021), https://doi.org/10.1016/j.cmet.2021.06.005

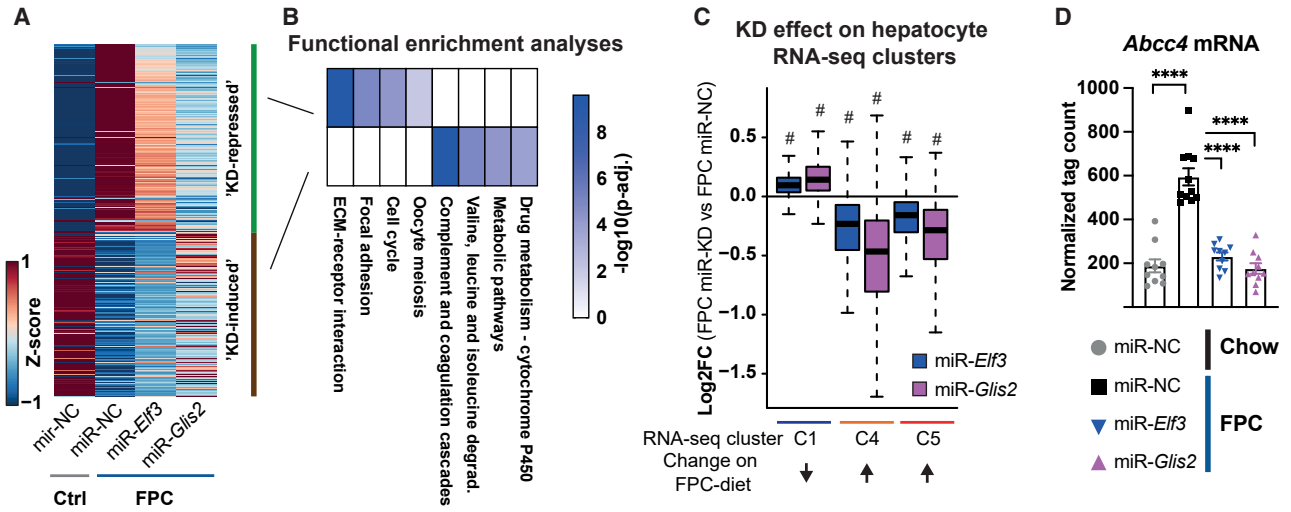

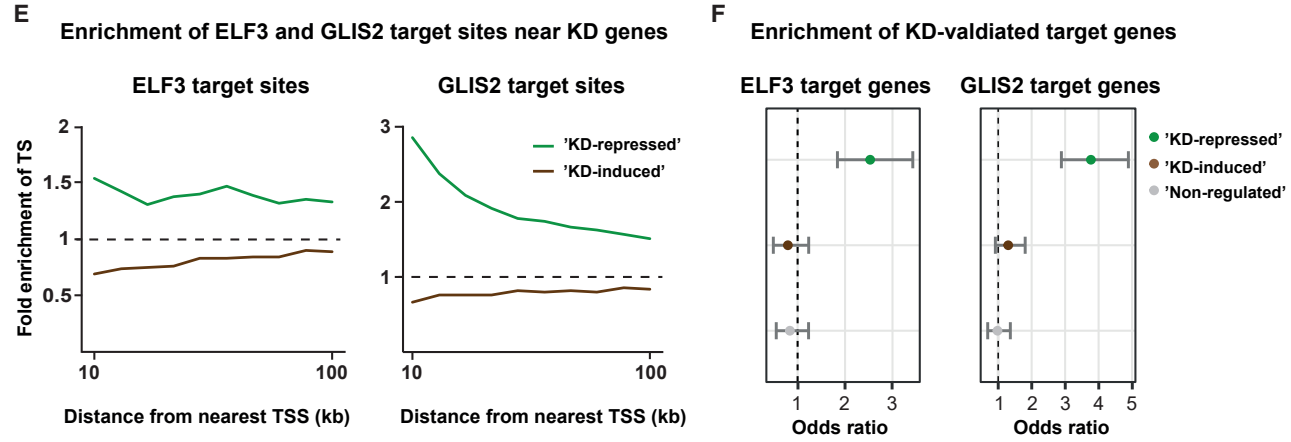

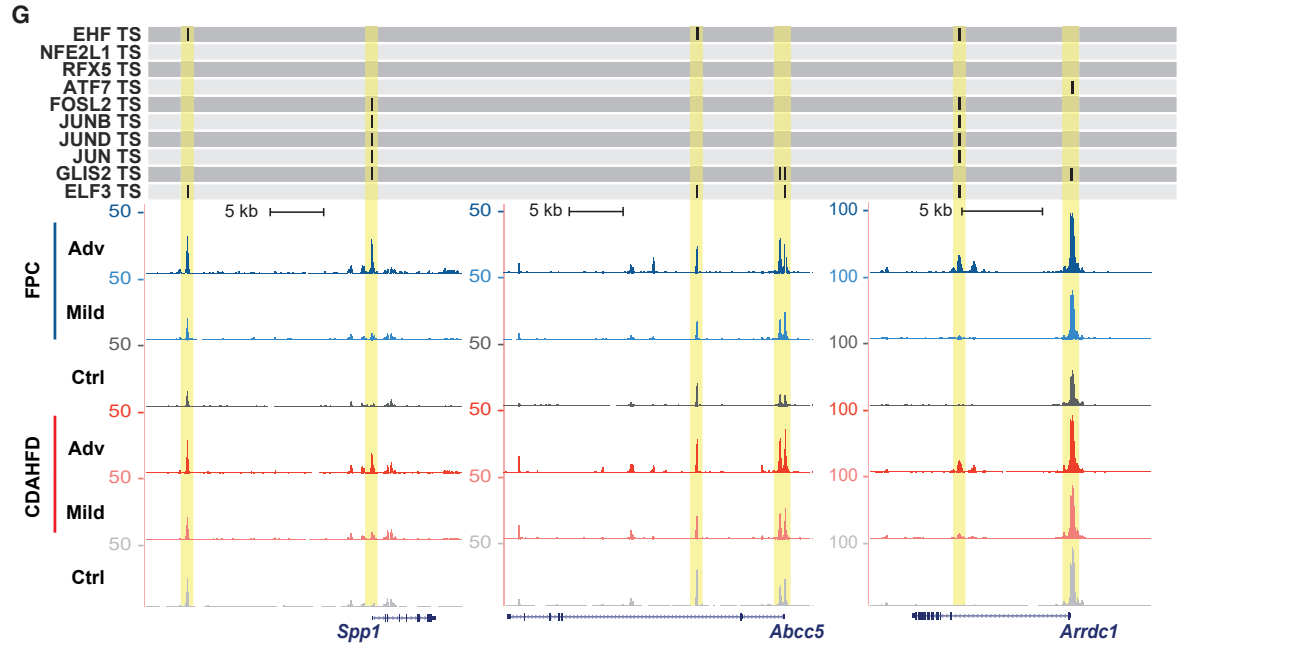

(legend on next page)

Please cite this article in press as: Loft et al., Liver-fibrosis-activated transcriptional networks govern hepatocyte reprogramming and intra-hepatic communication, Cell Metabolism (2021), https://doi.org/10.1016/j.cmet.2021.06.005

cell-cycle pathways, whereas FPC-repressed genes with impaired inhibition by *Elf3* and/or *Glis2* KD (i.e., KD-induced genes) were involved in complement and coagulation cascades and metabolic pathways (Figure 6A and 6B). This indicated that, overall, the KD of *Elf3* and *Glis2* affected the same hepatocyte genes and pathways that were specifically regulated in advanced NASH (Figures 6C and S6A). The loss of ELF3 and GLIS2 also modulated the expression of hepatocyte biomarkers for human liver fibrosis and poor prognosis of HCC, such as *Abcc4* (Figure 6D). Interestingly, *Elf3* and *Glis2* KD reversed the NASH-induced effect on hepatocyte identity genes, indicating that these factors contributed to the loss of hepatocyte identity during NASH progression (Figures S6B and S6C). Next, we combined information on dynamic genomic regions and target site prediction to identify the most likely regulatory ELF3 and GLIS2 target enhancers in NASH mice. We found that KD-repressed genes were specifically enriched for nearby ELF3 and GLIS2 target sites, but not for all dynamic genomic regions, compared with KD-induced genes (Figures 6E and S6D). Accordingly, ELF3 and GLIS2 target genes were highly enriched among KD-repressed genes compared with KD-induced genes as well as genes not affected by KD, implicating ELF3 and GLIS2 in the direct activation of this set of genes (Figure 6F). Of note, ELF3 and GLIS2 seemed to work on both different and common enhancers to regulate the KD-repressed genes during NASH progression, as exemplified in the loci of *Spp1*, *Abcc5*, and *Arrdc1*, which might also involve co-regulation by several other NASH-activated TFs (Figures 6G, S6E, and S6F).

ELF3 and GLIS2 modulate intra-hepatic crosstalk during NASH progression

We finally asked how *Elf3* and *Glis2* KD in hepatocytes affected gene expression in other hepatic cell populations during NASH development. Notably, *Elf3* and *Glis2* KD significantly modulated NASH-induced gene programs in LM and especially HSC, which included fibrosis-related signature genes of activated HSC (Figures 7A and 7B). In contrast, modest effects were observed in LEC and on NASH-repressed gene programs in all NPC populations (Figure S7A). Next, we used NicheNet analyses to predict hepatocyte SPP1 and connective tissue growth factor (CTGF) as the most likely mediators modulating the NASH-induced, KD-affected gene program in HSC (Figures 7C–7E). This was in line with our previous predictions and earlier studies highlighting these hepatokines as key mediators in the signaling between hepatocytes and HSC (Gressner et al., 2007; Zhu et al., 2018) targeting a hitherto unappreciated large NASH-induced gene program in HSC (Figure 7E). Notably, the motif activity of ELF3 and GLIS2 in hepatocytes strongly correlated with hepatocyte expression of both *Spp1* and *Ctgf* as well as the degree of fibrosis, but not steatosis in the NASH mice models (Figure 7F). Furthermore, in mouse and human cohorts, we also found significant correlations between the hepatic expression levels of *Elf3*, *Glis2*, and these hepatokines, as well as liver damage markers, inflammation, apoptosis, and fibrosis (Figures S7B and S7C). Finally, serum OPN levels (encoded by *Spp1*), which are a strong predictor of liver fibrosis in individuals diagnosed with MAFLD (Glass et al., 2018), were significantly reduced by *Elf3* and *Glis2* KD in NASH mice (Figure S7D).

DISCUSSION

By using a cell-type specific genomics approach, our study establishes a hepatocyte-centric view on NASH progression and highlights the biological relevance of key transcriptional nodes for hepatocyte function and intra-hepatic cell-to-cell communication in MALFD progression.

Our analyses show that the hepatocyte genome and transcriptome are dramatically altered in advanced NASH leading to a shutdown of core hepatocyte functions and the induction of cancer-related pathways. Intriguingly, in advanced NASH, the comprehensive reprogramming leads to a loss of hepatocyte identity. Loss of cellular identity has previously been demonstrated for resident liver macrophages in NASH (Seidman et al., 2020) and for hepatocytes in HCC, where adult hepatocytes have the capacity both to directly transform into cancer cells, or dedifferentiate into precursor cells that in turn develop into HCC cells (Sia et al., 2017). Our study highlights that a gradual and prominent transformation of hepatocytes is already initiated in the earlier stages of liver dysfunction, potentially priming the liver toward progressive dysfunction and eventually tumor development.

It is becoming increasingly clear that TFs are often part of bigger interconnected networks and we describe here a NASH-activated regulatory TF network likely to cooperate at

Figure 6. ELF3 and GLIS2 control NASH-activated hepatocyte gene programs

(A) Heatmap showing row-scaled and k-means clustered log2FC in expression (RNA-seq) of hepatocyte genes regulated by FPC feeding and affected by *Elf3* and/or *Glis2* knockdown (KD) ($p_{adj} < 0.01$).

(B) Functional enrichment analyses using KEGG pathways for the gene clusters.

(C) Log2FC in expression (FPC miRNA-*Elf3* or FPC miRNA-*Glis2* versus FPC miR-NC) for genes in the indicated RNA-seq gene cluster, as defined in Figure 1I.

(D) Expression (RNA-seq) of *Abcc4* in whole liver (n = 10–11).

(E) Enrichment of predicted ELF3 (left) and GLIS2 (right) target sites (TS) in the vicinity (i.e., 100 kb within the transcription start site (TSS) of FPC-induced, "KD-repressed" hepatocyte genes (green) or FPC-repressed, "KD-induced" hepatocyte genes (brown).

(F) Enrichment (as indicated by odds ratio) of ELF3 (left) and GLIS2 (right) target genes among FPC-induced, "KD-repressed" hepatocyte genes (green), FPC-repressed, "KD-induced hepatocyte" genes (brown), or hepatocyte genes not regulated by *Elf3* or *Glis2* KD (gray).

(G) UCSC genome browser screenshots showing predicted target sites (TS) of indicated NASH-activated TF (upper) and ATAC-seq read density in the *Spp1*, *Abcc5*, and *Arrdc1* loci in GFP+ nuclei from HEP INTACT mice (lower). (C) Horizontal line indicates the median and whiskers indicate 1.5× IQR. (D) Every dot/square/triangle represents one individual mouse. Bars indicate mean ± SEM. (F) The circle indicates odds ratio with 95% confidence interval. Significance was determined by (C) one-sample Wilcoxon signed rank test (mu = 0), (D) one-way ANOVA with Dunnett's multiple comparison test between FPC miR-NC mice and the other conditions or (F) using Fisher's exact test and indicated by the odds ratio. ****$p < 0.0001$, $^{\#}p < 1e^{-98}$, ns, non-significant.

See also Figure S6.

Please cite this article in press as: Loft et al., Liver-fibrosis-activated transcriptional networks govern hepatocyte reprogramming and intra-hepatic communication, Cell Metabolism (2021), https://doi.org/10.1016/j.cmet.2021.06.005

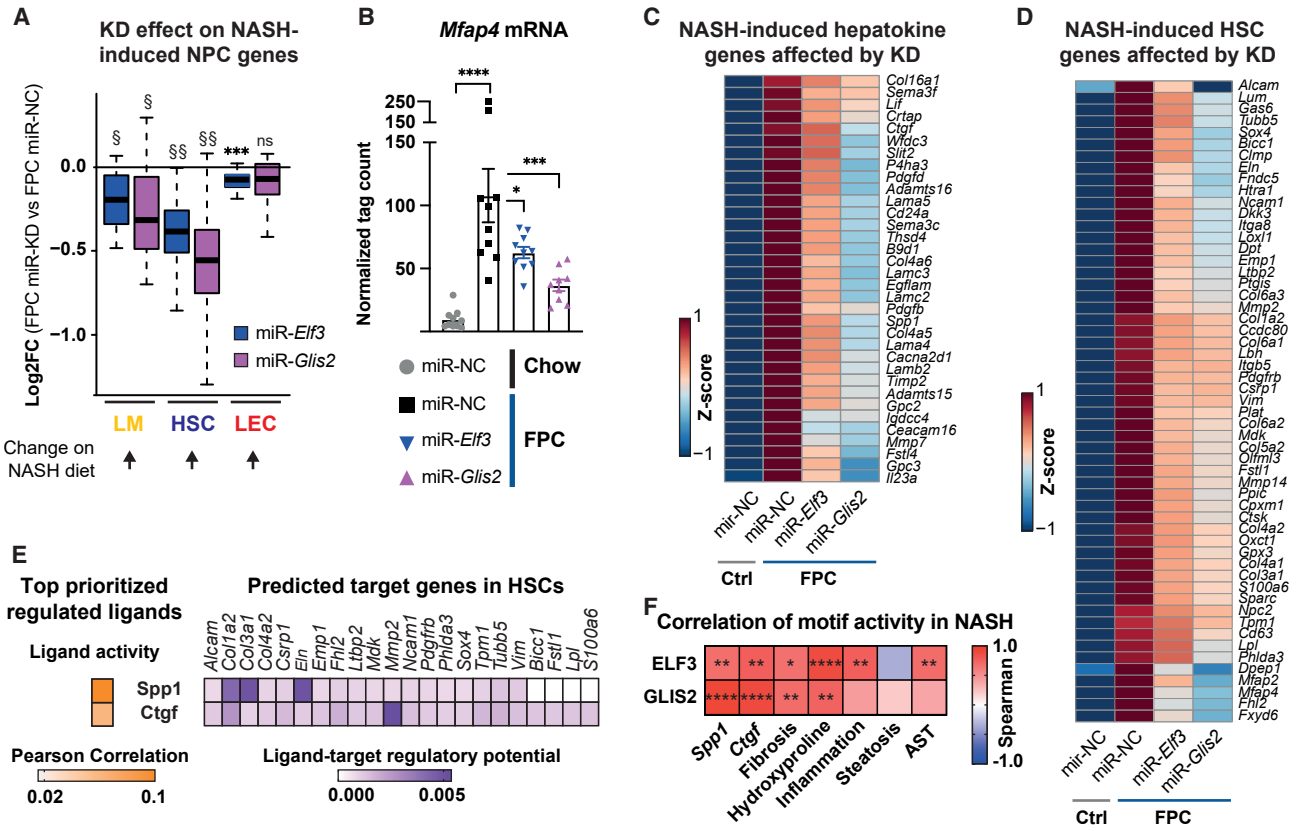

Figure 7. ELF3 and GLIS2 modulate hepatocyte-HSC crosstalk during NASH progression

(A) Log2FC in expression (FPC miRNA-*Elf3* or FPC miRNA-*Glis2* versus FPC miR-NC) for NASH-induced genes in liver macrophages (LM), hepatic stellate cells (HSC), and liver endothelial cells (LEC).

(B) Expression (RNA-seq) of *Mfap4* in whole liver (n = 10–11).

(C) Heatmap showing row-scaled expression values (RNA-seq) of FPC-induced, knockdown (KD)-regulated ($p_{adj} < 0.1$) genes encoding putative NASH-activated hepatokines.

(D) Heatmap showing row-scaled expression values (RNA-seq) of the FPC-induced, KD-regulated ($p_{adj} < 0.1$) HSC-associated gene program.

(E) NicheNet analysis of top prioritized hepatokines and their predicted target genes in HSC. Ligand activity of top predicted hepatokines (left), and the regulatory potential for the top predicted FPC-induced, KD-regulated ($p_{adj} < 0.1$) target genes associated with each hepatokine (right).

(F) Heatmap showing the Spearman correlation coefficient between ELF3 or GLIS2 motif activity in hepatocytes and the indicated parameter in NASH mouse models; *Spp1* and *Ctgf* hepatocyte expression (RNA-seq), fibrosis (Sirius red area in liver sections), hydroxyproline (hydroxyproline content in liver), inflammation (number of inflammatory foci/field in liver sections), steatosis (% fat area in liver sections), apoptosis (number of cleaved caspase-3-positive cells/field in liver sections), and AST (serum activity of aspartate aminotransferase).

(A) Horizontal line indicates the median and whiskers indicate 1.5× IQR. (B) Every dot/square/triangle represents one individual mouse. Bars indicate mean ± SEM. Significance was determined by (A) one-sample Wilcoxon signed rank test (mu = 0), (B) one-way ANOVA with Dunnett's multiple comparison test between FPC miR-NC mice and the other conditions, or (F) two-sided p value. *p < 0.05, **p < 0.01, ***p < 0.001, ****p < 0.0001, §p < 1e^{-5}, §§p < 1e^{-10}, ns, non-significant. See also Figure S7.

multiple levels. First, several of these TFs appear to be involved in the regulation of each other, which might further reinforce their activation during NASH progression. Second, these TFs seem to cooperate in the induction of at least a subset of NASH-activated enhancers and genes in the hepatocytes. And finally, the cooperative actions between the regulatory TFs also seem to be essential for NASH progression, since loss of network members, ELF3 and GLIS2, is able not only to alleviate the intracellular effect on the NASH-induced hepatocyte gene programs but also mitigate formation of fibrosis in the liver. GLIS2 has previously been implicated in kidney fibrosis development, in which pathways related to immune responses and fibrosis/tissue remodeling were activated in the kidneys of *Glis2*-deficient mice (Attanasio et al., 2007; Kim et al., 2008). It is likely that tissue- and context-dependent differences, including the available set of cooperating TFs, is responsible for the differential effects of GLIS2 on fibrosis-related gene expression in kidney and liver.

Recent studies have highlighted the contribution of HSC-derived stellakines to the regulation of LEC and LM functions in NASH (Xiong et al., 2019a) and our findings add hepatocytes as an important target of stellakine action in NASH. Moreover, we outline a NASH-induced hepatokine signature that targets HSC and, to some extent, LM and LEC disease-linked gene programs, further emphasizing the importance of hepatocyte dysfunction for organ-wide disease manifestation. The crosstalk between hepatocytes and NPCs is likely to reinforce the disease-associated

gene programs in the other hepatic cellular populations, leading to a vicious cycle of hepatokine, cytokine, and stellakine production, communally promoting NASH progression. The production of NASH-associated hepatokines seems to be under the tight transcriptional control of the NASH-activated hepatocyte TF network. Here, ELF3 and GLIS2 promote the induction of several hepatokine NASH signature genes, including *Spp1* and *Ctgf*, likely contributing to the activation of HSC and liver fibrosis development. Hepatocyte OPN (encoded by *Spp1*) and CTGF have previously been implicated in both NASH and acceleration of HCC (Gressner et al., 2007; Zhu et al., 2018), where OPN induces EMT in HCC cells (Dong et al., 2016). Since ELF3 promotes EMT and HCC progression in human HCC cell lines (Zheng et al., 2018), the regulation of *Spp1* in NASH livers might be a mechanism by which ELF3 contributes to the EMT in the advanced stages of NASH to promote a cancerous liver phenotype.

Together, our data outline an interconnected TF network that cooperatively governs NASH progression by controlling a program of hepatokines impacting on disease-activated genes in HSC. This emphasizes the importance of hepatocyte TF hubs as critical determinants not only of hepatocyte dysfunction but also of intra-hepatic crosstalk during NASH progression. This further persuades one to speculate that therapeutic targeting of such regulatory hubs specifically in NASH-activated hepatocytes, thereby interfering with the complex interconnected TF networks that determine NASH progression, could pave the way to a more effective drug design for treatment of NASH. By determining not only hepatocyte dysfunction but also connectivity to other hepatic cell types, combinatorial targeting strategies of TFs within these cooperative hubs may overcome the current difficulties to establish effective NASH therapies, which are mostly directed against single checkpoints.

Limitations of the study

Since our study mainly focused on key TFs and the transcriptional mechanisms involved in the progression of NASH, we did not capture important non-transcriptional mechanisms previously shown to be required for NASH progression (Wang et al., 2020). Furthermore, our target site analyses in the mouse liver were based on *in silico* predictions. Finally, with our current approaches, we have not been able to address the heterogeneity as well as the developmental origin of NASH-activated hepatocytes. Thus, a future combination of lineage-tracing studies, single-cell technologies, and subtype-specific targeting strategies will be needed to determine the significance of different hepatic epithelial subpopulations in NASH development.

STAR★METHODS

Detailed methods are provided in the online version of this paper and include the following:

SUPPLEMENTAL INFORMATION

Supplemental information can be found online at https://doi.org/10.1016/j.cmet.2021.06.005.

ACKNOWLEDGMENTS

We thank A. Rauch at SDU and L. Harrison at IDC for input to the manuscript. We acknowledge the team of technicians at IDC for assistance with mouse work, as well as E. Graf at HMGU and R. Nielsen at SDU for help with the sequencing. The graphical abstract was created with BioRender.com. This work was financially supported by grants from the Deutsche Forschungsgemeinschaft (DFG, German Research Foundation) through the Collaborative Research Center (CRC) 1118, project number 236360313 to S.H.; F.B.P., M.K.T., K.R., and B.B. are supported by the Danish National Research Foundation (grant DNRF141) to Center for Functional Genomics and Tissue Plasticity (ATLAS); M.P. and B.B. are supported by a grant from the Novo Nordisk Foundation (NNF) (NNF18OC0052768); S.F.S. (NNFOC150019050) and A.L. (NNF16OC0020742) are supported by fellowships from the NNF; A.L. is supported by the Danish Independent Research Council | Natural Sciences (DFF-6110-00265), an EMBO Long-Term Fellowship (ALTF 897-2015) and a DZD grant NEXT.

AUTHOR CONTRIBUTIONS

Conceptualization, A.L. and S.H.; methodology, A.L., S.F.S., and A.J.A.; formal analyses, A.L., A.J.A., F.B.P., M.K.T., M.P., and A.F.; investigation, A.L., A.J.A., S.F.S., F.B.P., M.P., K.K.C., A.B., M.T., and A.M.; resources, A.L., A.J.A., S.F.S., A.F., T.S., M.K.T., G.W., M.S., R.B., B.E.Ü., P.N., K.R., M.B.D., B.B., and S.H.; writing – original draft, A.L. and S.H.; writing – review and editing, A.L., A.J.A., S.F.S., and S.H.; visualization, A.L.; supervision, A.L., S.F.S, K.R., B.B., and S.H; project administration, A.L. and S.H.; funding acquisition, A.L. and S.H.

DECLARATION OF INTERESTS

The authors declare no competing interests.

Received: December 14, 2020
Revised: May 27, 2021
Accepted: June 9, 2021
Published: July 7, 2021

REFERENCES

Ægidius, H.M., Veidal, S.S., Feigh, M., Hallenborgh, P., Puglia, M., Pers, T.H., Vrang, N., Jelsing, J., Kornum, B.R., Blagoev, B., et al. (2020). Multi-omics characterization of a diet-induced obese model of non-alcoholic steatohepatitis. Sci Rep *10*, 1148.

Ahrens, M., Ammerpohl, O., von Schönfels, W., Kolarova, J., Bens, S., Itzel, T., Teufel, A., Herrmann, A., Brosch, M., Hinrichsen, H., et al. (2013). DNA methylation analysis in nonalcoholic fatty liver disease suggests distinct disease-specific and remodeling signatures after bariatric surgery. Cell Metab *18*, 296–302.

Angulo, P., Kleiner, D.E., Dam-Larsen, S., Adams, L.A., Bjornsson, E.S., Charatcharoenwitthaya, P., Mills, P.R., Keach, J.C., Lafferty, H.D., Stahler, A., et al. (2015). Liver fibrosis, but no other histologic features, is associated with long-term outcomes of patients With nonalcoholic fatty liver disease. Gastroenterology *149*, 389–397.e10.

Arriazu, E., Ge, X., Leung, T.M., Magdaleno, F., Lopategi, A., Lu, Y., Kitamura, N., Urtasun, R., Theise, N., Antoine, D.J., and Nieto, N. (2017). Signalling via the osteopontin and high mobility group box-1 axis drives the fibrogenic response to liver injury. Gut *66*, 1123–1137.

Attanasio, M., Uhlenhaut, N.H., Sousa, V.H., O'Toole, J.F., Otto, E., Anlag, K., Klugmann, C., Treier, A.C., Helou, J., Sayer, J.A., et al. (2007). Loss of GLIS2 causes nephronophthisis in humans and mice by increased apoptosis and fibrosis. Nat. Genet. *39*, 1018–1024.

Baeck, C., Wehr, A., Karlmark, K.R., Heymann, F., Vucur, M., Gassler, N., Huss, S., Klussmann, S., Eulberg, D., Luedde, T., et al. (2012). Pharmacological inhibition of the chemokine CCL2 (MCP-1) diminishes liver macrophage infiltration and steatohepatitis in chronic hepatic injury. Gut *61*, 416–426.

Balwierz, P.J., Pachkov, M., Arnold, P., Gruber, A.J., Zavolan, M., and van Nimwegen, E. (2014). ISMARA: automated modeling of genomic signals as a democracy of regulatory motifs. Genome Res *24*, 869–884.

Batth, T.S., Tollenaere, M.X., Rüther, P., Gonzalez-Franquesa, A., Prabhakar, B.S., Bekker-Jensen, S., Deshmukh, A.S., and Olsen, J.V. (2019). Protein aggregation capture on microparticles enables multipurpose proteomics sample preparation. Mol. Cell. Proteomics *18*, 1027–1035.

Benayoun, B.A., Pollina, E.A., Ucar, D., Mahmoudi, S., Karra, K., Wong, E.D., Devarajan, K., Daugherty, A.C., Kundaje, A.B., Mancini, E., et al. (2014). H3K4me3 breadth is linked to cell identity and transcriptional consistency. Cell *158*, 673–688.

Browaeys, R., Saelens, W., and Saeys, Y. (2020). NicheNet: modeling intercellular communication by linking ligands to target genes. Nat. Methods *17*, 159–162.

Butler, A., Hoffman, P., Smibert, P., Papalexi, E., and Satija, R. (2018). Integrating single-cell transcriptomic data across different conditions, technologies, and species. Nat. Biotechnol. *36*, 411–420.

Clapper, J.R., Hendricks, M.D., Gu, G., Wittmer, C., Dolman, C.S., Herich, J., Athanacio, J., Villescaz, C., Ghosh, S.S., Heilig, J.S., et al. (2013). Diet-induced mouse model of fatty liver disease and nonalcoholic steatohepatitis reflecting clinical disease progression and methods of assessment. Am. J. Physiol. Gastrointest. Liver Physiol. *305*, G483–G495.

Cox, J., and Mann, M. (2008). MaxQuant enables high peptide identification rates, individualized p.p.b.-range mass accuracies and proteome-wide protein quantification. Nat. Biotechnol. *26*, 1367–1372.

Deal, R.B., and Henikoff, S. (2010). A simple method for gene expression and chromatin profiling of individual cell types within a tissue. Dev. Cell *18*, 1030–1040.

Dobie, R., Wilson-Kanamori, J.R., Henderson, B.E.P., Smith, J.R., Matchett, K.P., Portman, J.R., Wallenborg, K., Picelli, S., Zagorska, A., Pendem, S.V., et al. (2019). Single-cell transcriptomics uncovers zonation of function in the mesenchyme during liver fibrosis. Cell Rep *29*, 1832–1847.e8.

Dobin, A., Davis, C.A., Schlesinger, F., Drenkow, J., Zaleski, C., Jha, S., Batut, P., Chaisson, M., and Gingeras, T.R. (2013). STAR: ultrafast universal RNA-seq aligner. Bioinformatics *29*, 15–21.

Dong, Q., Zhu, X., Dai, C., Zhang, X., Gao, X., Wei, J., Sheng, Y., Zheng, Y., Yu, J., Xie, L., et al. (2016). Osteopontin promotes epithelial-mesenchymal transition of hepatocellular carcinoma through regulating vimentin. Oncotarget *7*, 12997–13012.

du Plessis, J., van Pelt, J., Korf, H., Mathieu, C., van der Schueren, B., Lannoo, M., Oyen, T., Topal, B., Fetter, G., Nayler, S., et al. (2015). Association of Adipose Tissue Inflammation With Histologic Severity of Nonalcoholic Fatty Liver Disease. Gastroenterology *149*, 635–648.

Dubois, V., Gheeraert, C., Vankrunkelsven, W., Dubois-Chevalier, J., Dehondt, H., Bobowski-Gerard, M., Vinod, M., Zummo, F.P., Güiza, F., Ploton, M., et al. (2020). Endoplasmic reticulum stress actively suppresses hepatic molecular identity in damaged liver. Mol. Syst. Biol. *16*, e9156.

Feuchtinger, A., Stiehler, T., Jütting, U., Marjanovic, G., Luber, B., Langer, R., and Walch, A. (2015). Image analysis of immunohistochemistry is superior to visual scoring as shown for patient outcome of esophageal adenocarcinoma. Histochem. Cell Biol. *143*, 1–9.

Frades, I., Andreasson, E., Mato, J.M., Alexandersson, E., Matthiesen, R., and Martinez-Chantar, M.L. (2015). Integrative genomic signatures of hepatocellular carcinoma derived from nonalcoholic Fatty liver disease. PLoS One *10*, e0124544.

Friedman, S.L., Neuschwander-Tetri, B.A., Rinella, M., and Sanyal, A.J. (2018). Mechanisms of NAFLD development and therapeutic strategies. Nat. Med. *24*, 908–922.

Fujii, M., Shibazaki, Y., Wakamatsu, K., Honda, Y., Kawauchi, Y., Suzuki, K., Arumugam, S., Watanabe, K., Ichida, T., Asakura, H., and Yoneyama, H. (2013). A murine model for non-alcoholic steatohepatitis showing evidence of association between diabetes and hepatocellular carcinoma. Med. Mol. Morphol. *46*, 141–152.

Glass, O., Henao, R., Patel, K., Guy, C.D., Gruss, H.J., Syn, W.K., Moylan, C.A., Streilein, R., Hall, R., Mae Diehl, A., et al. (2018). Serum interleukin-8, osteopontin, and monocyte chemoattractant protein 1 are associated with hepatic fibrosis in patients with nonalcoholic fatty liver disease. Hepatol. Commun. *2*, 1344–1355.

Gressner, O.A., Lahme, B., Demirci, I., Gressner, A.M., and Weiskirchen, R. (2007). Differential effects of TGF-beta on connective tissue growth factor (CTGF/CCN2) expression in hepatic stellate cells and hepatocytes. J. Hepatol. *47*, 699–710.

Gu, Z., Gu, L., Eils, R., Schlesner, M., and Brors, B. (2014). circlize Implements and enhances circular visualization in R. Bioinformatics *30*, 2811–2812.

Hasenfuss, S.C., Bakiri, L., Thomsen, M.K., Williams, E.G., Auwerx, J., and Wagner, E.F. (2014). Regulation of steatohepatitis and PPARgamma signaling by distinct AP-1 dimers. Cell Metab *19*, 84–95.

Heinz, S., Benner, C., Spann, N., Bertolino, E., Lin, Y.C., Laslo, P., Cheng, J.X., Murre, C., Singh, H., and Glass, C.K. (2010). Simple combinations of lineage-determining transcription factors prime cis-regulatory elements required for macrophage and B cell identities. Mol. Cell *38*, 576–589.

Jones, A., Friedrich, K., Rohm, M., Schäfer, M., Algire, C., Kulozik, P., Seibert, O., Müller-Decker, K., Sijmonsma, T., Strzoda, D., et al. (2013). TSC22D4 is a molecular output of hepatic wasting metabolism. EMBO Mol. Med. *5*, 294–308.

Kanehisa, M., Sato, Y., Furumichi, M., Morishima, K., and Tanabe, M. (2019). New approach for understanding genome variations in KEGG. Nucleic Acids Res *47*, D590–D595.

Kim, Y.S., Kang, H.S., Herbert, R., Beak, J.Y., Collins, J.B., Grissom, S.F., and Jetten, A.M. (2008). Kruppel-like zinc finger protein Glis2 is essential for the maintenance of normal renal functions. Mol. Cell. Biol. *28*, 2358–2367.

Kita, Y., Takamura, T., Misu, H., Ota, T., Kurita, S., Takeshita, Y., Uno, M., Matsuzawa-Nagata, N., Kato, K., Ando, H., et al. (2012). Metformin prevents and reverses inflammation in a non-diabetic mouse model of nonalcoholic steatohepatitis. PLoS One *7*, e43056.

Krenkel, O., Hundertmark, J., Abdallah, A.T., Kohlhepp, M., Puengel, T., Roth, T., Branco, D.P.P., Mossanen, J.C., Luedde, T., Trautwein, C., et al. (2020). Myeloid cells in liver and bone marrow acquire a functionally distinct inflammatory phenotype during obesity-related steatohepatitis. Gut *69*, 551–563.

Kulozik, P., Jones, A., Mattijssen, F., Rose, A.J., Reimann, A., Strzoda, D., Kleinsorg, S., Raupp, C., Kleinschmidt, J., Müller-Decker, K., et al. (2011). Hepatic deficiency in transcriptional cofactor TBL1 promotes liver steatosis and hypertriglyceridemia. Cell Metab *13*, 389–400.

Lange, V., Picotti, P., Domon, B., and Aebersold, R. (2008). Selected reaction monitoring for quantitative proteomics: a tutorial. Mol. Syst. Biol. *4*, 222.

Layer, R.M., Pedersen, B.S., DiSera, T., Marth, G.T., Gertz, J., and Quinlan, A.R. (2018). GIGGLE: a search engine for large-scale integrated genome analysis. Nat. Methods *15*, 123–126.

Lefebvre, P., Lalloyer, F., Bauge, E., Pawlak, M., Gheeraert, C., Dehondt, H., Vanhoutte, J., Woitrain, E., Hennuyer, N., Mazuy, C., et al. (2017). Interspecies NASH disease activity whole-genome profiling identifies a fibrogenic role of PPARalpha-regulated dermatopontin. JCI Insight *2*.

Li, H., and Durbin, R. (2009). Fast and accurate short read alignment with Burrows-Wheeler transform. Bioinformatics *25*, 1754–1760.

Li, H., Handsaker, B., Wysoker, A., Fennell, T., Ruan, J., Homer, N., Marth, G., Abecasis, G., and Durbin, R.; 1000 Genome Project Data Processing Subgroup (2009). The sequence alignment/Map format and SAMtools. Bioinformatics *25*, 2078–2079.

Loft, A., Forss, I., and Mandrup, S. (2017). Genome-wide insights into the development and function of thermogenic adipocytes. Trends Endocrinol. Metab. *28*, 104–120.

Love, M.I., Huber, W., and Anders, S. (2014). Moderated estimation of fold change and dispersion for RNA-seq data with DESeq2. Genome Biol *15*, 550.

MacLean, B., Tomazela, D.M., Shulman, N., Chambers, M., Finney, G.L., Frewen, B., Kern, R., Tabb, D.L., Liebler, D.C., and MacCoss, M.J. (2010). Skyline: an open source document editor for creating and analyzing targeted proteomics experiments. Bioinformatics *26*, 966–968.

Madsen, J.G., Schmidt, S.F., Larsen, B.D., Loft, A., Nielsen, R., and Mandrup, S. (2015). iRNA-seq: computational method for genome-wide assessment of acute transcriptional regulation from total RNA-seq data. Nucleic Acids Res *43*, e40.

Madsen, J.G.S., Rauch, A., Van Hauwaert, E.L., Schmidt, S.F., Winnefeld, M., and Mandrup, S. (2018). Integrated analysis of motif activity and gene expression changes of transcription factors. Genome Res *28*, 243–255.

Matsumoto, M., Hada, N., Sakamaki, Y., Uno, A., Shiga, T., Tanaka, C., Ito, T., Katsume, A., and Sudoh, M. (2013). An improved mouse model that rapidly develops fibrosis in non-alcoholic steatohepatitis. Int. J. Exp. Pathol. *94*, 93–103.

Meex, R.C.R., and Watt, M.J. (2017). Hepatokines: linking nonalcoholic fatty liver disease and insulin resistance. Nat. Rev. Endocrinol. *13*, 509–520.

Merrell, A.J., Peng, T., Li, J., Sun, K., Li, B., Katsuda, T., Grompe, M., Tan, K., and Stanger, B.Z. (2021). Dynamic transcriptional and epigenetic changes drive cellular plasticity in the liver. Hepatology. https://doi.org/10.1002/hep.31704.

Mo, A., Mukamel, E.A., Davis, F.P., Luo, C., Henry, G.L., Picard, S., Urich, M.A., Nery, J.R., Sejnowski, T.J., Lister, R., et al. (2015). Epigenomic signatures of neuronal diversity in the mammalian brain. Neuron *86*, 1369–1384.

Moylan, C.A., Pang, H., Dellinger, A., Suzuki, A., Garrett, M.E., Guy, C.D., Murphy, S.K., Ashley-Koch, A.E., Choi, S.S., Michelotti, G.A., et al. (2014). Hepatic gene expression profiles differentiate presymptomatic patients with mild versus severe nonalcoholic fatty liver disease. Hepatology *59*, 471–482.

Nathwani, A.C., Gray, J.T., Ng, C.Y., Zhou, J., Spence, Y., Waddington, S.N., Tuddenham, E.G., Kemball-Cook, G., McIntosh, J., Boon-Spijker, M., et al. (2006). Self-complementary adeno-associated virus vectors containing a novel liver-specific human factor IX expression cassette enable highly efficient transduction of murine and nonhuman primate liver. Blood *107*, 2653–2661.

Niu, L., Thiele, M., Geyer, P.E., Rasmussen, D.N., Webel, H.E., Santos, A., Gupta, R., Meier, F., Strauss, M., Kjaergaard, M., et al. (2020). A paired liver biopsy and plasma proteomics study reveals circulating biomarkers for alcohol-related liver disease. bioRxiv. https://doi.org/10.1101/2020.10.16.337592.

Perez-Riverol, Y., Csordas, A., Bai, J., Bernal-Llinares, M., Hewapathirana, S., Kundu, D.J., Inuganti, A., Griss, J., Mayer, G., Eisenacher, M., et al. (2019). The PRIDE database and related tools and resources in 2019: improving support for quantification data. Nucleic Acids Res *47*, D442–D450.

Peterson, A.C., Russell, J.D., Bailey, D.J., Westphall, M.S., and Coon, J.J. (2012). Parallel reaction monitoring for high resolution and high mass accuracy quantitative, targeted proteomics. Mol. Cell. Proteomics *11*, 1475–1488.

Postic, C., Shiota, M., Niswender, K.D., Jetton, T.L., Chen, Y., Moates, J.M., Shelton, K.D., Lindner, J., Cherrington, A.D., and Magnuson, M.A. (1999). Dual roles for glucokinase in glucose homeostasis as determined by liver and pancreatic beta cell-specific gene knock-outs using Cre recombinase. J. Biol. Chem. *274*, 305–315.

Ramachandran, P., Dobie, R., Wilson-Kanamori, J.R., Dora, E.F., Henderson, B.E.P., Luu, N.T., Portman, J.R., Matchett, K.P., Brice, M., Marwick, J.A., et al. (2019). Resolving the fibrotic niche of human liver cirrhosis at single-cell level. Nature *575*, 512–518.

Ramachandran, P., Matchett, K.P., Dobie, R., Wilson-Kanamori, J.R., and Henderson, N.C. (2020). Single-cell technologies in hepatology: new insights into liver biology and disease pathogenesis. Nat. Rev. Gastroenterol. Hepatol. *17*, 457–472.

Rauch, A., Haakonsson, A.K., Madsen, J.G.S., Larsen, M., Forss, I., Madsen, M.R., Van Hauwaert, E.L., Wiwie, C., Jespersen, N.Z., Tencerova, M., et al. (2019). Osteogenesis depends on commissioning of a network of stem cell transcription factors that act as repressors of adipogenesis. Nat. Genet. *51*, 716–727.

Remmerie, A., Martens, L., Thoné, T., Castoldi, A., Seurinck, R., Pavie, B., Roels, J., Vanneste, B., De Prijck, S., Vanhockerhout, M., et al. (2020). Osteopontin expression identifies a subset of recruited macrophages distinct from Kupffer cells in the fatty liver. Immunity *53*, 641–657.e14.

Rose, A.J., Berriel Diaz, M., Reimann, A., Klement, J., Walcher, T., Krones-Herzig, A., Strobel, O., Werner, J., Peters, A., Kleyman, A., et al. (2011). Molecular control of systemic bile acid homeostasis by the liver glucocorticoid receptor. Cell Metab *14*, 123–130.

Sachs, S., Niu, L., Geyer, P., Jall, S., Kleinert, M., Feuchtinger, A., Stemmer, K., Brielmeier, M., Finan, B., DiMarchi, R.D., et al. (2021). Plasma proteome profiles treatment efficacy of incretin dual agonism in diet-induced obese female and male mice. Diabetes Obes. Metab. *23*, 195–207.

Sanchez-Quiles, V., Akimov, V., Osinalde, N., Francavilla, C., Puglia, M., Barrio-Hernandez, I., Kratchmarova, I., Olsen, J.V., and Blagoev, B. (2017). Cylindromatosis tumor suppressor protein (CYLD) deubiquitinase is necessary for proper ubiquitination and degradation of the epidermal growth factor receptor. Mol. Cell. Proteomics *16*, 1433–1446.

Schwabe, R.F., Tabas, I., and Pajvani, U.B. (2020). Mechanisms of fibrosis development in nonalcoholic steatohepatitis. Gastroenterology *158*, 1913–1928.

Seidman, J.S., Troutman, T.D., Sakai, M., Gola, A., Spann, N.J., Bennett, H., Bruni, C.M., Ouyang, Z., Li, R.Z., Sun, X., et al. (2020). Niche-specific reprogramming of epigenetic landscapes drives myeloid cell diversity in nonalcoholic steatohepatitis. Immunity *52*, 1057–1074.e7.

Sia, D., Villanueva, A., Friedman, S.L., and Llovet, J.M. (2017). Liver cancer cell of origin, molecular class, and effects on patient prognosis. Gastroenterology *152*, 745–761.

Siersbæk, M., Varticovski, L., Yang, S., Baek, S., Nielsen, R., Mandrup, S., Hager, G.L., Chung, J.H., and Grøntved, L. (2017). High fat diet-induced changes of mouse hepatic transcription and enhancer activity can be reversed by subsequent weight loss. Sci. Rep. *7*, 40220.

Si-Tayeb, K., Lemaigre, F.P., and Duncan, S.A. (2010). Organogenesis and development of the liver. Dev. Cell *18*, 175–189.

Stefan, N., and Häring, H.U. (2013). The role of hepatokines in metabolism. Nat. Rev. Endocrinol. *9*, 144–152.

Terkelsen, M.K., Bendixen, S.M., Hansen, D., Scott, E.A.H., Moeller, A.F., Nielsen, R., Mandrup, S., Schlosser, A., Andersen, T.L., Sorensen, G.L., et al. (2020). Transcriptional dynamics of hepatic sinusoid-associated cells After liver injury. Hepatology *72*, 2119–2133.

Wang, S., Sun, H., Ma, J., Zang, C., Wang, C., Wang, J., Tang, Q., Meyer, C.A., Zhang, Y., and Liu, X.S. (2013). Target analysis by integration of transcriptome and ChIP-seq data with BETA. Nat. Protoc. *8*, 2502–2515.

Tsuchida, T., Lee, Y.A., Fujiwara, N., Ybanez, M., Allen, B., Martins, S., Fiel, M.I., Goossens, N., Chou, H.I., Hoshida, Y., et al. (2018). A simple diet- and chemical-induced murine NASH model with rapid progression of steatohepatitis, fibrosis and liver cancer. J Hepatol *69*, 385–395.

Wang, X., Cai, B., Yang, X., Sonubi, O.O., Zheng, Z., Ramakrishnan, R., Shi, H., Valenti, L., Pajvani, U.B., Sandhu, J., et al. (2020). Cholesterol stabilizes TAZ in hepatocytes to promote experimental non-alcoholic steatohepatitis. Cell Metab *31*, 969–986.e7.

Wang, X., Zheng, Z., Caviglia, J.M., Corey, K.E., Herfel, T.M., Cai, B., Masia, R., Chung, R.T., Lefkowitch, J.H., Schwabe, R.F., and Tabas, I. (2016). Hepatocyte TAZ/WWTR1 promotes inflammation and fibrosis in nonalcoholic steatohepatitis. Cell Metab *24*, 848–862.

Whyte, W.A., Orlando, D.A., Hnisz, D., Abraham, B.J., Lin, C.Y., Kagey, M.H., Rahl, P.B., Lee, T.I., and Young, R.A. (2013). Master transcription factors and mediator establish super-enhancers at key cell identity genes. Cell *153*, 307–319.

Xia, J., Yuan, J., Xin, L., Zhang, Y., Kong, S., Chen, Y., Yang, S., and Li, K. (2014). Transcriptome analysis on the inflammatory cell infiltration of nonalcoholic steatohepatitis in bama minipigs induced by a long-term high-fat, high-sucrose diet. PLoS One *9*, e113724.

Xiong, X., Kuang, H., Ansari, S., Liu, T., Gong, J., Wang, S., Zhao, X.Y., Ji, Y., Li, C., Guo, L., et al. (2019a). Landscape of intercellular crosstalk in healthy and NASH liver revealed by single-cell secretome gene analysis. Mol. Cell *75*, 644–660.e5.

Xiong, X., Wang, Q., Wang, S., Zhang, J., Liu, T., Guo, L., Yu, Y., and Lin, J.D. (2019b). Mapping the molecular signatures of diet-induced NASH and its regulation by the hepatokine Tsukushi. Mol. Metab. *20*, 128–137.

Young, M.D., Wakefield, M.J., Smyth, G.K., and Oshlack, A. (2010). Gene ontology analysis for RNA-seq: accounting for selection bias. Genome Biol *11*, R14.

Younossi, Z., Anstee, Q.M., Marietti, M., Hardy, T., Henry, L., Eslam, M., George, J., and Bugianesi, E. (2018). Global burden of NAFLD and NASH: trends, predictions, risk factors and prevention. Nat. Rev. Gastroenterol. Hepatol. *15*, 11–20.

Zheng, L., Xu, M., Xu, J., Wu, K., Fang, Q., Liang, Y., Zhou, S., Cen, D., Ji, L., Han, W., and Cai, X. (2018). ELF3 promotes epithelial-mesenchymal transition by protecting ZEB1 from miR-141-3p-mediated silencing in hepatocellular carcinoma. Cell Death Dis *9*, 387.

Zhu, C., Kim, K., Wang, X., Bartolome, A., Salomao, M., Dongiovanni, P., Meroni, M., Graham, M.J., Yates, K.P., Diehl, A.M., et al. (2018). Hepatocyte Notch activation induces liver fibrosis in nonalcoholic steatohepatitis. Sci. Transl. Med. *10*.

Please cite this article in press as: Loft et al., Liver-fibrosis-activated transcriptional networks govern hepatocyte reprogramming and intra-hepatic communication, Cell Metabolism (2021), https://doi.org/10.1016/j.cmet.2021.06.005

STAR★METHODS

KEY RESOURCES TABLE

REAGENT or RESOURCE	SOURCE	IDENTIFIER
Antibodies		
Rabbit monoclonal anti-GFP antibody	Life Technologies	Cat: G10362; RRID:AB_2536526
Rabbit monoclonal anti-F4/80 antibody [CI:A3-1]	Abcam	Cat: ab6640; RRID:AB_1140040
Goat anti-Rat IgG (H+L) Cross-Adsorbed Secondary Antibody, DyLight 550	Thermo Fisher Scientific	Cat: SA5-10019; RRID:AB_2556599
Rabbit monoclonal anti-Cleaved Caspase-3 [5A1E]	Cell Signaling Technologies	Cat: 9664; RRID: AB_2070042
Biotinylated Goat anti-Rabbit IgG antibody	Vector Laboratories	Cat: BA-1000; RRID: AB_2313606
Bacterial and virus strains		
AAV2/8-LP1-GFPmut-miRNA-NC	Kulozik et al, 2011; Rose et al, 2011	N/A
AAV2/8-LP1-GFPmut-miRNA-*Elf3*	This work	N/A
AAV2/8-LP1-GFPmut-miRNA-*Glis2*	This work	N/A
Biological samples		
Liver from 10wks old STAM™ mice and age-matched controls.	SMC laboratories	N/A
Liver from mice fed a methionine, choline-deficient diet and low-fat control diet for 4 wks.	Jones et al., 2013	N/A
Chemicals, peptides, and recombinant proteins		
TRIzol	Life Technologies	15596018
EDTA-free protease inhibitor	Roche	11873580001
RNasin® Plus Rnase Inhibitor	Promega	N2615
Igepal CA-630	Sigma	56741
Protein G Dynabeads	Life Technologies	10004D
Hoechst33342	Thermo Fisher Scientific	H1399
DAPI	Sigma	D9542
Synthetic peptide for Elf3: TQVLEWISYQVE K(+8)	Synpeptide	N/A
Synthetic peptide for Elf3: LVFGP LGDQLHAQL R(+10)	Synpeptide	N/A
Synthetic peptide for Elf3: DILIHPELNEGLM K(+8)	Synpeptide	N/A
Synthetic peptide for Elf3: SEAVAQLWGQ K(+8)	Synpeptide	N/A
Synthetic peptide for Glis2: ELGLVDDSP APGSPGSPPPGFLLNP K(+8)	Synpeptide	N/A
Synthetic peptide for Glis2: YLDGVPSSFQ FFLPLGSGGALHLPASSFLPPP K(+8)	Synpeptide	N/A
Synthetic peptide for Glis2: CLSPELPLA K(+8)	Synpeptide	N/A
Synthetic peptide for Glis2: NPLLPSPFGA GGLGLPVVSLLGGSAGS K(+8)	Synpeptide	N/A
Critical commercial assays		
AST Activity Assay Kit	Sigma	MAK055-1KT
Mouse /Rat Osteopontin (OPN) Quantikine ELISA kit	R&D Systems	MOST00
Sensitive Tissue Collagen Assay	Quickzyme	QZBtiscol1
QuantiTect Reverse Transcription Kit	Qiagen	205311
VAHTS Stranded mRNA-seq Library Kit for Illumina	Vazyme	NR602
NEBNext® Ultra™ RNA Library Prep Kit for Illumina®	New England Biolabs	E7530L
Truseq Stranded mRNA	Illumina	20020595

(*Continued on next page*)

Please cite this article in press as: Loft et al., Liver-fibrosis-activated transcriptional networks govern hepatocyte reprogramming and intra-hepatic communication, Cell Metabolism (2021), https://doi.org/10.1016/j.cmet.2021.06.005

Continued

REAGENT or RESOURCE	SOURCE	IDENTIFIER
TruePrep™ DNA Library Prep Kit V2 for Illumina	Vazyme	TD501
MinElute Reaction Cleanup kit	Qiagen	28204
Pierce™ BCA Protein Assay Kit	Thermo Fisher Scientific	23225
Discovery® DAB Map Kit	Ventana Medical Systems	760-124
Deposited data		
Liver microarray data set of a human cohort of individuals grouped into control, healthy obese and NASH	Ahrens et al., 2013	GEO: GSE48452
Liver microarray data set of a human cohort of individuals diagnosed with MAFLD having a fibrosis score from 0-1 (mild) or 3-4 (advanced)	Moylan et al., 2014	GEO: GSE49541
Liver microarray data of a human cohort consisting of 2 patient groups, group I (< 5 % steatosis) and group III (NASH)	du Plessis et al., 2015	GEO: GSE59045
Liver microarray data set of a human cohort of individuals grouped into control and NASH	Frades et al., 2015	GEO: GSE63067
Liver microarray data set of a human cohort of individuals grouped into control and NASH	Lefebvre et al., 2017	GEO: GSE83452
Liver microarray data set of mice fed a methionine- and choline-deficient + high fat diet or a control low-fat diet for 8 wks.	Kita et al., 2012	GEO: GSE35961
Liver RNA-seq data set of control low fat diet-fed mice, CCl_4-treated mice at 12 wks and western diet-fed + CCl_4-treated mice at 24 weeks.	Tsuchida et al., 2018	GEO: GSE99010
Liver RNA-seq data set of control low fat diet-fed and Amylin Liver NASH diet-fed mice for 36 wks.	Xiong et al., 2019b	GEO: GSE119340
RNA-seq data set of Bama minipigs fed with control diet or with high-fat, high-sucrose diet for 23 mo.	Xia et al., 2014	SRA: SRX197296
RNA-seq data of control, injured and reprogrammed mouse hepatocytes isolated from control mice and mice with DDC-induced liver injury.	Merrell et al., 2021	GEO: GSE156894
INTACT RNA-seq data	This work	GEO: GSE162876
INTACT ATAC-seq data	This work	GEO: GSE162870
Whole liver RNA-seq data of FPC-fed mice with *Elf3* or *Glis2* KD	This work	GEO: GSE162869
Whole liver RNA-seq data from NASH mouse models	This work	GEO: GSE162863
Nuclear proteomics dataset	This work	PRIDE: PXD025691
Source data	This work	Mendeley: https://doi.org/10.17632/bc28kstdvx.1
Experimental models: organisms/strains		
B6;129-Gt(ROSA) 26Sor$^{tm5(CAG-Sun1/sfGFP)Nat}$ / J mice	JAX	Stock: 021039
B6N.Cg-Speer6-ps1$^{Tg(Alb-cre)21Mgn}$ / J	JAX	Stock: 018961
Oligonucleotides		
qPCR primers	This work	Table S5
miRNA-targeting oligoes	This work	Table S5
Recombinant DNA		
Plasmid: pdsAAV-LP1-GFPmut-miRNA-NC	Kulozik et al, 2011; Rose et al, 2011	N/A
Plasmid: pdsAAV-LP1-GFPmut-miRNA-*Elf3*	This work	N/A
Plasmid: pdsAAV-LP1-GFPmut-miRNA-*Glis2*	This work	N/A

(*Continued on next page*)

Please cite this article in press as: Loft et al., Liver-fibrosis-activated transcriptional networks govern hepatocyte reprogramming and intra-hepatic communication, Cell Metabolism (2021), https://doi.org/10.1016/j.cmet.2021.06.005

Continued

REAGENT or RESOURCE	SOURCE	IDENTIFIER
Software and algorithms		
STAR	Dobin et al., 2013	v2.4.2a
BWA aligner	Li and Durbin, 2009	v0.7.5a-r405
Samtools	Li et al., 2009	v0.1.19-44428cd
iRNA-seq	Madsen et al., 2015	v1.1
DESeq2	Love et al., 2014	v1.24.0
HOMER	Heinz et al., 2010	v4.10
IMAGE	Madsen et al., 2018	v1.1
GOseq	Young et al., 2010	v1.36.0
ISMARA	Balwierz et al., 2014	https://ismara.unibas.ch/mara/
KEGG PATHWAY database collection	Kanehisa et al., 2019	https://www.genome.jp/kegg/
BETA	Wang et al., 2013	http://cistrome.org/BETA/
NicheNet	Browaeys et al., 2020	v0.1.0
Circlize	Gu et al., 2014	v0.4.9
Definiens Developer XD	Definiens AG	v2.0
Prism	Graphpad	9.1.0
R	https://www.r-project.org/	3.6.2
Other		
Rodent chow pellets	Altromin	1314
Fructose, palmitate and cholesterol (FPC) diet	Research Diet	D17020104
L-amino-defined high (60 kcal %) fat, choline-deficient diet with 0.1% methionine (CDAHFD)	Research Diet	A06071302
10% low fat diet	Research Diet	A06071314
AMPure XP beads	Beckman	A63881
EconoSpin Micro/Mini Columns	Epoch	3010-250/1920-250
100um CellTrics filter unit	Sysmex Deutschland GmbH	04-0042-2318
70μm cell strainer	Greiner Bio-one	542070

RESOURCE AVAILABILITY

Lead contact

Further information and requests for resources and reagents should be directed to and will be fulfilled by the lead contact, Stephan Herzig (Stephan.herzig@helmholtz-muenchen.de).

Materials availability

New reagents (e.g., plasmids) generated in this study are listed in the key resource table and will be made available on request, but we may require a completed Materials Transfer Agreement if there is potential for commercial application.

Data and code availability

Raw and processed sequencing data generated in this study have been deposited in the NCBI GEO database. The mass spectrometry proteomics data have been deposited to the ProteomeXchange Consortium via the PRIDE (Perez-Riverol et al., 2019) partner repository. This paper analyzes existing, publicly available data. All accession numbers for the datasets are listed in the key resources table. Additional source data and information required to reanalyze the findings reported in this paper is available from the lead contact and will be made accessible via Mendeley https://doi.org/10.17632/bc28kstdvx.1 upon request.

EXPERIMENTAL MODEL DETAILS

Animal models and experiments

All animal studies were conducted in accordance with German animal welfare legislation and protocols were approved by the state ethics committee and government of Upper Bavaria (no. 55.2-1-55-2532-49-2017). All mice were maintained in a climate-controlled environment at approximately 23°C and constant humidity with specific pathogen-free conditions under strict 12 h dark–light cycles (6:00 a.m. to 6:00 p.m.). All mice had *ad libitum* access to food and water and before the start of experiments and all mice were

maintained on a standard chow diet (Altromin, 1314). For generation of HEP-INTACT mice, *B6;129-Gt(ROSA)26Sor*$^{tm5(CAG-Sun1/sfGFP)Nat}$*/J* mice (Mo et al., 2015) were backcrossed to C57BL/6N (B6N) using speed congenics to ensure a > 95 % genetic B6N background and then crossed with the *B6N.Cg-Speer6-ps1*$^{Tg(Alb-cre)21Mgn}$*/J* (Alb-Cre) (Postic et al., 1999) mice. For feeding experiments, body weight-matched male littermates were randomly assigned to experimental groups and grouped-housed with two mice in each cage. In one study, 6-7 wk old male HEP-INTACT male mice were fed a fructose-palmitate-cholesterol (FPC) diet (Research Diet, D17020104) essentially formulated as previously described (Wang et al., 2016) with drinking water containing 42 g/L glucose and fructose (55 % / 45 %, w/w) or a standard chow control diet for 20 wks. In another study, 6-7 wk old male HEP-INTACT mice were fed an L-amino-defined high (60 kcal %) fat diet with 0.1 % methionine and no added choline (CDAHFD, Research Diet A06071302) or a control low fat diet (Research Diet A06071314) matched for total calories for 7 weeks, formulated as previously described (Matsumoto et al., 2013). For the AAV-mediated knock down studies, 6-7 week old male HEP-INTACT mice were fed either the FPC diet or a control diet for 14 weeks. Aspartate aminotransferase (AST) activity was measured in plasma obtained from the tail-vein and mice receiving the FPC diet were grouped into three groups with matching body weights and AST activity. Mice were tail-vein injected with either AAV2/8-LP1-GFPmut-miRNA-NC, AAV2/8-LP1-GFPmut-miRNA-*Elf3* or AAV2/8-LP1-GFPmut-miRNA-*Glis2* ($5x10^{11}$ p.f.u./mouse) and kept additionally 10 weeks on the diet. For all mouse experiments, the health status of mice was monitored, and weight was recorded at least once per week and all mice used for experiments displayed good general health. During the mouse experiment, animal caretakers and investigators conducting the experiments were generally not blinded to the group allocation of mice. The total number of mice analyzed for each experiment is detailed in the figure legends.

We obtained livers from different NASH mouse models for RNA-seq analyses. Here livers from 10week old STAM™ mice (Fujii et al., 2013) and age-matched controls were purchased from the SMC laboratories (JAPAN). Finally, livers from mice fed a methionine, choline-deficient diet for 4 week and low fat diet controls were obtained from a previous study (Jones et al., 2013).

METHOD DETAILS

Generation of adeno-associated virus (AAV)

Specific miRNA oligoes targeting *Elf3* or *Glis2* were selected using the BLOCK-iT™ RNAi Designer (Thermo Fisher Scientific). AAVs encoding miRNA targeting *Elf3* [termed miR-*Elf3*] or *Glis2* [termed miR-*Glis2*] under the control of the hepatocyte-specific LP1 promoter (Nathwani et al., 2006) were prepared essentially as previously described (Kulozik et al., 2011; Rose et al, 2011), except that the production of recombinant viruses and determination of virus titer were performed by Vigene Biosciences. A previously designed AAV containing a non-targeting miRNA [termed miR-NC] was used as control (Kulozik et al., 2011).

Isolation of GFP-tagged nuclei

Liver tissue from INTACT mice was rapidly dissected in PBS and snap-frozen in liquid nitrogen. The tissue was crushed into fine powder using a Tissuelyzer II (Qiagen) and subsequently washed in PBS. The tissue was dounce homogenized using 10x loose pestle in 5 mL of low sucrose buffer (LSB: 0.25 M sucrose, 25 mM KCl, 5 mM MgCl2, 20 mM Tricine-HCL (pH 7.5), 1 mM 1,4-dithiothreitol (DTT), 0.15 mM spermine, 0.5 mM spermidine, 1x EDTA-free protease inhibitor (Roche), and 60 U/mL RNasin® Plus Rnase Inhibitor (Promega) per 0.5 mg of tissue, then added 0.35 % Igepal CA-630 (Sigma) and left on ice for 5 min followed by further douncing 5x with the tight pestle. The homogenate was filtered through a 100 μm CellTrics filter unit (Sysmex Deutschland) and spun down at 600g for 10 min at 4 °C. The pellet was resuspended in 9x high sucrose buffer (HSB; same as LSB, but with 2 M sucrose) and centrifuged at 15,000g for 15 min at 4 °C. The nuclei pellet was subsequently resuspended in wash buffer (LSB with 0.35 % Igepal) and an aliquot of whole liver nuclei was kept on ice for later analyses. Pre-clearing of nuclei (15 million nuclei per HEP-INTACT mouse) was done by incubating with 20 μL of Protein G Dynabeads (Life Technologies) for 15 min. After magnetic removal of the beads, the solution was incubated with 3 μg of rabbit monoclonal anti-GFP antibody (Life Technologies) for 30 min. Then 80 μL of Dynabeads was added and the solution was incubated for an additional 20 min. Bead-bound nuclei were washed 3x in 2 mL wash buffer (without RNasin) using a magnet. All steps were performed on ice or in the cold room (4 °C) and all incubations were carried out using an end-to-end rotator. For determination of the fraction of GFP+ nuclei in livers of control and NASH mice, 100-200 nuclei obtained from whole livers were counted using a fluorescence microscope, calculating the ratio between GFP+ and DAPI-stained nuclei.

Serum and liver metabolite measurements

Blood levels of glucose were determined directly via blood from the tail vein using an automatic glucose monitor ACCU-Chek (Roche). Alanine aminotransferase (ALT) and AST activity as well as concentration of albumin, cholesterol, low-density lipoprotein (LDL), high-density lipoprotein (HDL), and triacylglycerol (TG) were measured in serum using the relevant assays on a 480U Chemistry Analyzer (Beckmann Coulter). For measurement of AST activity in plasma an AST Activity Assay Kit was used (Sigma Aldrich) and for quantification of serum osteopontin (OPN) a mouse/rat OPN Quantikine ELISA kit (R&D systems) was used. For detection of liver hydroxyproline content, approximately 50 mg of liver tissue was completely hydrolyzed in 6 M HCl at 95 °C for 20 hrs in a thermoblock and subsequently centrifuged for 10 min at 13,000g. The supernatant was diluted with H_2O to a final concentration of 4 M HCl and then used for measuring the concentration of hydroxyproline residues with a Sensitive Tissue Collagen Assay (Quickzyme) in accordance with manufacturer's recommendations. The hydroxyproline content was normalized to mg wet tissue weight.

Please cite this article in press as: Loft et al., Liver-fibrosis-activated transcriptional networks govern hepatocyte reprogramming and intra-hepatic communication, Cell Metabolism (2021), https://doi.org/10.1016/j.cmet.2021.06.005

Histology

Excised liver samples were fixed in 4 % (w/v) neutrally buffered formalin, embedded in paraffin and cut into 3 μm consecutive slices for haematoxylin and eosin (H&E) and Sirius red staining as well as staining of cleaved caspase-3. Immunohistochemical stainings were performed under standardized conditions on a Discovery XT automated stainer (Ventana Medical Systems) using monoclonal rabbit anti-cleaved caspase-3 (1:250, Cell Signaling Technologies) as a primary antibody and goat anti-rabbit, biotinylated (1:750) (Vector Laboratories) as secondary antibody. Signal detection was conducted using the Discovery® DAB Map Kit (Ventana Medical Systems). For F4/80 immunoreactivity, 12 μm sections of snap frozen liver tissue were fixed for 5 min in 4 % (w/v) neutrally buffered formalin before staining with monoclonal rat anti-F4/80 (1:200, Abcam) and detecting with Dylight 550-conjugated goat anti-rat (1:100, Thermo Fisher Scientific). Nuclei were counterstained with Hoechst 33342 (Thermo Fisher Scientific). For the F4/80 immunostainings, 2-3 samples in each group were excluded due to insufficient sample quality. The stained tissue sections were scanned with an AxioScan.Z1 digital slide scanner (Zeiss) equipped with a 20x magnification objective.

Automated digital image analyses

Automated digital image analyses (Definiens Developer XD 2, Definiens AG) were used for evaluation of stained liver sections as previously described (Feuchtinger et al., 2015; Sachs et al., 2021). Quantification of the lipid amount was morphometrically determined on H&E-stained liver sections. The calculated parameter was the percentage of surface area considered as lipid vacuoles, divided by the surface area of the entire analyzed liver tissue for each sample. Additionally, the degree of fibrosis was digitally determined and defined as the percentage of Sirius red positive stained tissue area per total analyzed liver tissue area. For the F4/80 stainings, the number of F4/80 positive cells per mm^2 liver tissue was digitally determined.

Quantification of inflammation and apoptosis

The number of inflammatory foci and cleaved caspase-3-positive hepatocytes were counted manually in fields at 20x magnification with 5-10 fields of systematically sliding views per case. An inflammatory focus was defined by the presence of > 4 mononuclear cells in the H&E-stained section profiles in close proximity inside the hepatic parenchyma.

Preparation of nuclear protein lysates

100-300 mg of liver tissue was carefully minced followed by dounce homogenizing using 10-20x loose pestle and 10x tight pestle in 4 mL LSB with 0.2 % Igepal CA-630 (Sigma). The homogenate was filtered through a 70 μm mesh and spun down at 500g for 10 min at 4 °C. The nuclei pellet was resuspended in 9x HSB, centrifuged at 15,000g for 15 min at 4 °C and washed one time in LSB. To extract the nuclear proteins, pellets was resuspended in 50 μL of LSB followed by addition of an equal volume of NUN buffer (Tricine-HCL (pH 8), 2M urea, 600 mM NaCl, 1 mM DTT, 1x EDTA-free protease) and incubated on ice for 30 min. Finally, the nuclear extract was spun at 16,000g for 20 min at 4 °C and protein concentration was determined using the BCA assay (Thermo Fisher Scientific).

Targeted nuclear proteomics

Nuclear lysates (~10 μg of protein) were treated in denaturing buffer (8 M guanidine hydrochloride in 25 mM ammonium bicarbonate) at 95 °C for 5 min. On-bead protein aggregation (Batth et al., 2019) was induced using magnetic HILIC beads (ReSyn Biosciences (Pty) Ltd.), 70 % (v/v) acetonitrile (ACN) and 30 min of incubation with shaking at room temperature. Bead bound protein aggregates were retained using a magnet and the supernatant was removed before washing once with pure ACN and once with 70 % (v/v) ethanol. Protein aggregates were diluted in 100 μL of 50 mM ammonium bicarbonate, reduced with 2 mM DTT for 30 min and alkylated with 11 mM chloracetamide for 30 min in the dark. Following proteolytic digestion with 1:200 of LysC (Wako) for 1 hour at 37 °C, samples were digested with 1:100 of trypsin (Promega) overnight at 37 °C, and subsequently oxidized using 0.05 % (v/v) hydrogen peroxide. After acidification with trifluoroacetic acid, samples were desalted on C18 StageTips, eluates were vacuum-dried in a speed-vac and resuspended in 10 μL of 0.5 % (v/v) acetic acid.

Unique peptide sequences from ELF3 (Q3UPW2) and GLIS2 (Q8VDL9) to be targeted using parallel reaction monitoring (PRM)-mass spectrometry (Peterson et al., 2012) were selected based on a combination of previous mass spectrometric results registered in the PeptideAtlas (http://www.peptideatlas.org), PABST peptide rankings, and general recommendations for selecting peptides (Lange et al., 2008). Synthetic peptides were purchased from Synpeptide Co., Ltd (Shanghai, China) with heavy-isotope labelling of the C-terminal amino acid, being either arginine +10 Da or lysine +8 Da. Synthetic peptides were dissolved in varying concentrations of ACN, pooled together in equimolar amounts, and diluted 1:100 in 50 mM ammonium bicarbonate to reduce the concentration of ACN. Peptides were prepared by reduction, alkylation, oxidization, acidification, desalting, vacuum-drying, and resuspension, as described above. Approximately 0.5 μg of digested nuclear protein extract was loaded along with 1 picomol of synthetic peptides onto an LC-MS/MS system consisting in an Exploris 480 Mass Spectrometer (Thermo Fischer Scientific), coupled with an EASY-nLC 1000 (Thermo Fischer Scientific). Reverse phase (RP) chromatography was performed on a 20-cm analytical column, packed in house with ReproSil Pur C_{18}-AQ 1.9 μm resin (Dr Maisch GmbH). The nano-HPLC was operating with an ACN/water solvent system containing 0.5 % acetic acid at a flow rate of 0.25 μL per min. Peptide RP separation was achieved using a step-gradient from 4 to 8 % ACN for 7 min, followed by a slow gradient to 30 % ACN for 86 min, a ramp to 55 % ACN for 25 min and a plateau of 80 % ACN for 5 min. A PRM inclusion list containing the mass over charge (m/z) of the peptides used for quantitation in their heavy (synthetic) and light (endogenous) forms was uploaded in the Exploris 480 PRM method editor. After a full MS survey scan from 350 to 1500 m/z, at 60,000 resolution, with a maximum injection time of 50 ms and normalized automatic gain control (AGC)

Please cite this article in press as: Loft et al., Liver-fibrosis-activated transcriptional networks govern hepatocyte reprogramming and intra-hepatic communication, Cell Metabolism (2021), https://doi.org/10.1016/j.cmet.2021.06.005

target of 300 %, the MS/MS spectra of the target peptides were acquired in unscheduled PRM mode, using a resolution of 60,000, quadrupole isolation window of 1.6 Da, HCD collision energy of 30 % and an AGC target of 200 % with a maximum injection time of 110 ms.

Data analysis was performed, as previously described (Sanchez-Quiles et al., 2017), using Skyline™ 20.2.0.343 software (MacLean et al., 2010) with minor modifications. Briefly, after building a spectral library using MaxQuant v.1.6.2.3 (Cox and Mann, 2008), PRM acquired raw files were imported in Skyline software with MS1 and MS/MS filtering resolving power set to 60,000 and mass analyzer as Orbitrap. MS/MS filtering was set as targeted, and retention time filtering was set to include all matching scans. In peptide settings, carbamidomethyl cysteine and oxidation of methionine was set as fixed and variable modification, respectively. After using the retention time and fragmentation patterns of the synthetic peptides as a reference, MS/MS area fragment values relative to 3 – 5 fragment ions for each of the ELF3 and GLIS2 endogenous peptides were used for quantitation and exported for statistical analysis. Raw quantitation values were normalized among different runs using the area under the curve of full MS total ion current measured in Thermo Xcalibur v.4.4.16.14 (Thermo Fischer Scientific).

RNA isolation and quantitative PCR analysis

Liver tissue was homogenized directly in TRIzol using a Tissuelyzer II (Qiagen). Whole liver nuclei and bead-bound nuclei prepared from INTACT mice were directly resuspended in TRIzol. RNA purification was performed using EconoSpin columns (Epoch) with on-column DNase digestion (Qiagen) and cDNA was transcribed using the QuantiTect Reverse Transcription Kit (Qiagen). qPCR was conducted using SYBR™ Green PCR Master Mix (Life technologies, Darmstadt, Germany) and the reaction was performed using the QuantStudio6 system (Life technologies, Darmstadt, Germany). qPCR expression data were normalized to *Tbp* expression.

RNA-seq library construction and sequencing

For RNA-seq of nuclei from INTACT mice, total RNA (50-100 ng) was prepared for sequencing using VAHTS Stranded mRNA-seq Library Kit for Illumina (Vazyme) following manufacturer's recommendations, except that no selection for poly-adenylated RNA was applied. For RNA-seq of whole livers, libraries were constructed using the NEBNext Ultra RNA Library Prep Kit for Illumina (NEB) or Truseq Stranded mRNA (Illumina) following manufacturers' protocols. The prepared libraries were paired end sequenced (2x 50 bp) on the HiSeq 4000 or NovaSeq 6000 platform (Illumina).

ATAC-seq library construction and sequencing

Approximately 25,000 bead-bound nuclei from INTACT animals were transposed in a 50 μL volume of 1x TTBL buffer and 3.5 μL TTE Mix V50 (TruePrep™ DNA Library Prep Kit V2 for Illumina, Vazyme) for 30 min at 37 °C. Fragmented genomic DNA was recovered using Buffer ERC coupled with MinElute spin column purification (Qiagen). Transposed genomic DNA was amplified by 12 cycles of quantitative PCR. Amplified DNA was purified and size-selected on AMPure XP beads (Beckman), analyzed on an Agilent Bioanalyzer, and sequenced (paired-end) on the Illumina HiSeq 4000 platform.

Processing and analyses of RNA-seq data

For RNA-seq libraries, the STAR aligner (v2.4.2a) (Dobin et al., 2013) was used for split-read alignment against the mouse genome assembly mm10 and UCSC knownGene annotation. Quantification of the number of mapped reads of each gene was performed using iRNA-seq (v1.1) (Madsen et al., 2015) specifying the "-count gene" option. DESeq2 (v1.24.0) (Love et al., 2014) was used to determine differential gene expression (P_{adj} < 0.001, pairwise comparison) between the experimental conditions in one or both NASH models with ''independentFiltering'' set as FALSE. Whole liver nuclei-specific genes were filtered away from the gene list before further analyses and a set of non-regulated genes were defined as having P_{adj} > 0.2 in all pairwise comparisons. All genes regulated between one or more of the conditions were subjected to k-means clustering using 5 clusters and the ''average'' clustering method. Functional enrichment analyses of genes were performed with GO-seq (v1.36.0) (Young et al., 2010) using KEGG PATHWAY database collection (Kanehisa et al., 2019) excluding KEGG pathways under human diseases (i.e., 05XXX).

NicheNet ligand activity & secretome analyses

To explore the signaling from NPCs to hepatocytes in NASH, we first defined a set of potentially active ligands in the NPC population. For this, single cell gene expression data from LM, LEC, and HSC of mice with carbon tetrachloride (CCl_4)-induced liver fibrosis was used (Terkelsen et al., 2020) only considering genes expressed in at least 5 % of the cells in the defined cluster of the particular cell type. NASH-induced NPC ligands were selected as being induced in one or more of the cell types at one or more time points during CCl_4-induced fibrosis (Veh vs CCl_{4wk}/ CCl_{4wk}, $P < 1e^{-05}$, Wilcoxon Rank Sum test) as well as being induced in whole liver of the FPC and CDAHFD NASH models (P_{adj} < 0.1, control vs advanced NASH). Database information on ligand-receptor interactions was downloaded from https://zenodo.org/record/3260758/files/lr_network.rds and all NASH-induced NPC ligands for which at least one hepatocyte receptor was expressed (average mean expression over all conditions > 1tag/kb) was considered for further analyses. NicheNet (v0.1.0) (Browaeys et al., 2020) was used to rank the ligands based on how well they predicted if a gene belonged to a gene set of interest compared to a background gene set. The gene set of interest in hepatocytes was defined as genes selectively induced in advanced NASH in both our NASH mouse models (P_{adj} < 0.1, control and mild NASH vs advanced NASH) contained in RNA-seq cluster 4 or 5 and belonging to one or more of the following KEGG gene sets: cell cycle (mmu04110), MAPK signaling pathway (mmu04010), focal adhesion (mmu04510), and ECM-receptor interaction (mmu04512). As a background gene list, all other

Please cite this article in press as: Loft et al., Liver-fibrosis-activated transcriptional networks govern hepatocyte reprogramming and intra-hepatic communication, Cell Metabolism (2021), https://doi.org/10.1016/j.cmet.2021.06.005

genes expressed in the hepatocyte population (average mean expression over all conditions > 1tag/kb) was used. Ligand activity scores were calculated as the Pearson correlation coefficient between the ligand-target regulatory potential scores of each selected ligand and the target indicator vector, which indicated whether a gene belonged to the gene set of interest or not. For the ligands with highest ligand activity, a ligand-receptor potential score was calculated that reflected the weight of the interaction between the ligand and receptor in the weighted ligand signaling network downloaded from https://zenodo.org/record/3260758/files/weighted_networks.rds. For the NASH-induced NPC ligands, the most prominent hepatocyte target genes were selected based on the regulatory potential score if they belonged to the gene set of interest and to the 400 most strongly predicted targets of at least one of the ligands. Ligand-target gene and ligand-receptor interactions were displayed in a circle plot using the R-package 'circlize' (v0.4.9) (Gu et al., 2014). For visualization purposes, interaction links belonging to the 66 % of lowest scores were removed.

To explore the signaling from hepatocytes to NPCs in NASH, we performed NicheNet analyses essentially as described above. From a comprehensive mouse secretome gene database (Xiong et al., 2019a), we compiled a set of putative hepatokines selective induced in advanced NASH in both our NASH mouse models ($P_{adj} < 0.1$, control or mild NASH vs advanced NASH). The gene set of interest in NPCs was defined as genes regulated in one or more cell types of mice with CCl_4-induced NASH using Seurat (v2.3.4) FindMarkers (Butler et al., 2018) between the vehicle condition and 4 wks of CCl_4 treatment with default settings (i.e., identifying differentially expressed genes between the two groups using the Wilcoxon Rank Sum test and a $\log_2$ fold change threshold of 0.25). Furthermore, the NPC gene set of interest was confirmed to be induced in whole livers with advanced NASH in both our NASH mouse models ($P_{adj} < 0.1$, control or mild NASH vs advanced NASH). The background list of genes expressed in NPCs was defined as genes expressed in at least 5 % of the defined cluster of one or more cell types. Interactions between the top 10 prioritized hepatokines and the most prominent target genes belonging to the gene set of interest and to the 2000 most strongly predicted targets of at least one of the ligands were displayed in a circle plot. We also displayed the interactions between the top prioritized hepatokines and their target NPC receptors assigned to a given cell type if the gene encoding the receptor was expressed in at least 5 % of the defined cluster of the particular cell type.

Processing and analyses of ATAC-seq data

Sequence tags from ATAC-seq libraries were aligned to the mm10 using the BWA aligner (v0.7.5a-r405) (Li and Durbin, 2009). Post-alignment processing of reads was performed with Samtools (v0.1.19-44428cd) (Li et al., 2009) by removing duplicate reads and selecting for high quality reads using Samtools view using the following settings "-b -h -f 1 -F 4 -F 8 -F 256 -F 2048 -q 30". Furthermore, only reads with a fragment length < 100 bp were kept for further analyses corresponding to the reads located in nucleosome-free regions. ATAC seq peaks were identified, annotated and tags in peaks were counted using HOMER (v4.10) (Heinz et al., 2010). For visualization purposes, the individual tag directories of one condition were merged into one combined tag directory and bedgraphs were generated using HOMER makeUCSCfile specifying '-fragLength 70' and '-fsize 20e'. For identification of ATAC-seq peaks, peaks were called in each library with HOMER findPeaks using the following settings: 'peaks', '-fragLength 70', '-style factor', '-minDist 140', '-size 70'. For all peak files, overlapping peaks were merged and collected in one master peak file. Tags were then counted in a 200 bp window around the peak centers for each individual library in the master peak file. From this peak file mitochondrial peaks were removed, and high confident peaks were identified as having at least 15 tags per 200 bp window for all 3-4 replicates in at least one of the conditions. A similarity heatmap of all conditions was generated by correlating the ATAC-seq tag count for all identified ATAC-seq sites (i.e., 68,827 sites) using the Spearman correlation coefficient. Dynamic enhancers were identified using DESeq2 as ATAC-seq peaks being regulated ($P_{adj} < 0.001$, pairwise comparison) in one or more experimental conditions in one or both NASH mouse models with ''independentFiltering'' set as FALSE. For separation of hepatocyte peaks into superenhancers (SE) and typical enhancers (TE) identified in the control condition, individual tag directories from all control conditions were combined into one and HOMER findPeaks was used specifying the -style super and -typical options. The same strategy was applied for identifying NASH-associated SE using combined tag directories from the advanced NASH conditions. SE and TE were annotated to the nearest expressed gene (i.e., genes with a replicate average of fragments per kilobase per million mapped fragments > 0.5 in at least one of the conditions) and the log2FC in expression between the advanced NASH and control conditions for SE- and TE-associated genes was examined.

TF motif activity, target sites and genes

The relative contribution of TF motifs to enhancer activity and gene expression in a given condition was computed using IMAGE (v1.1) (Madsen et al., 2018) that applies a motif response analyses approach to integrate enhancer (ATAC-seq) and gene expression (RNA-seq) data. Thus, the activity of a particular motif for a given sample was calculated by estimating the average contribution of that motif to the activity of all identified enhancers. Motifs predicted to be causal (score 1 or 2) by IMAGE was tested for differential motif activity ($P_{adj} < 0.01$) between the advanced NASH state and the control and/or mild NASH state in one or both NASH mouse models using an unpaired, two-tailed student t-test corrected by the Benjamini–Hochberg method. Putative key regulators of NASH were identified using the top 25 motifs with highest motif activity in the advanced NASH state (averaged over both NASH mouse models). From this list, top 10 putative regulators were selected as being the TFs with the highest gain in motif activity from the mild NASH to the advanced NASH state (averaged over both NASH mouse models) that also displayed higher motif activity in the advanced NASH vs control condition. For the top predicted NASH-activated TFs, putative target sites (TS) were defined based on the ATAC-seq data from control and NASH mouse livers and the computational predictions made in IMAGE (Madsen et al., 2018). For JUN, the predicted TS were validated by calculating the similarity between the predicted peak set and the comprehensive collection of TF

Please cite this article in press as: Loft et al., Liver-fibrosis-activated transcriptional networks govern hepatocyte reprogramming and intra-hepatic communication, Cell Metabolism (2021), https://doi.org/10.1016/j.cmet.2021.06.005

sequencing data from the Cistrome Data Browser (CistromeDB) using the GIGGLE score (Layer et al., 2018) via the CistromeDB toolkit (http://dbtoolkit.cistrome.org/). The enrichment of TS in dynamic enhancers specifically regulated in the advanced NASH condition in comparison to non-dynamic enhancers for an increasing number of the key regulatory TFs was calculated, essentially as previously described (Rauch et al., 2019): $Enrichment_{TS} = log_2 \frac{\frac{TS\ in\ E\_NASH\_Dyn}{Size(E\_NASH\_Dyn)}}{\frac{TS\ in\ nonDynE}{Size(nonDynE)}}$, where E_NASH_Dyn denoted the group of dynamic enhancers in advanced NASH and nonDynE was non-dynamic enhancer sites (i.e., ATAC-seq sites that did not change accessibility during NASH progression). The log2FC in accessibility of all predicted TS (advanced NASH vs the control condition) for an increasing number of the NASH-activated TFs was evaluated.

For the top predicted TFs, putative target genes (TG) were identified using IMAGE and it was evaluated if the TFs cooperated in regulating the TG from distinct RNA-seq clusters over random. This was done by calculating the enrichment of IMAGE-predicted TG (and non-regulated genes) in the 5 RNA-seq k-means clusters, essentially as previously described (Rauch et al., 2019): $Enrichment_{TG} = log_2 \frac{TG\ in\ RNA-seq\ cluster}{TG * \frac{Size(RNA-seq\ cluster)}{Size(all\ expressed\ genes)}}$ for an increasing number of the predicted key TFs in comparison to a random distribution. Furthermore, the log2FC in expression of TG (advanced NASH vs the control condition) belonging to the RNA-seq cluster 5 for an increasing number of assigned regulatory TFs was evaluated. To further explore the TG of the top predicted regulatory TFs, BETA (Wang et al., 2013) (*34*) was used to score TG using either mouse INTACT ATAC-seq data or publicly available ChIP-seq data generated in the human HCC cell line, HEPG2, from CistromeDB.

The motif activity of the regulatory TFs in human liver biopsies was evaluated using 'integrated system for motif activity response analysis' (ISMARA) that estimates motif activity in gene promoter-proximal regions based on input expression data (Balwierz et al., 2014). For this, raw microarray CEL files retrieved from GSE48452 (Ahrens et al., 2013) and GSE49541 (Moylan et al., 2014) was used. We grouped individuals in each study into two groups based on the NASH diagnosis, NAS score and/or fibrosis score. The individuals from GSE48452 were assigned to the control group if they were diagnosed as control or healthy obese and had NAS and fibrosis scores = 0. Alternatively, they were assigned to the NASH group if diagnosed with NASH and had a NAS score > 3 and a fibrosis score $\geq$ 1. For individuals from GSE49541, the control group contained 40 individuals diagnosed with mild fibrosis that had a fibrosis score $\leq$ 1, whereas the advanced fibrosis group contained 32 individuals diagnosed with advanced NASH that had a fibrosis score $\geq$ 3.

Bioinformatics analyses of Elf3 and Glis2 KD

DESeq2 was used to identify genes regulated by FPC feeding ($P_{adj} < 0.01$, FPC miRNA-NC group vs Control miRNA-NC group) that additionally were regulated by one or both of the KD conditions ($P_{adj} < 0.01$, FPC miRNA-NC group vs FPC miRNA-KD). This set of genes was subjected to k-means clustering using the ''average'' clustering method. The effect of *Elf3* and *Glis2* KD on NASH-induced apoptosis-associated gene expression was evaluated on genes contained in the KEGG apoptotic pathway (mmu04210) significantly induced ($P_{adj} < 0.01$, $log_2FC > 1$) by FPC feeding. For testing the impact of *Elf3* and *Glis2* KD on inflammatory subpopulations, a panel of marker genes for inflammatory cellular subpopulations was obtained that had been assigned based on CITE-seq of CD45+ immune cells in the livers of mice with MAFLD (Remmerie et al., 2020).

The enrichment of IMAGE-predicted ELF3 and GLIS2 TS was determined as the number of TS per gene within different distances from the transcription start site (TSS; 10–100 kb) of FPC-regulated, KD-affected genes relative to the number of TS per gene of all expressed hepatocyte genes. The odds ratio was used to evaluate the significance of overlap between predicted ELF3 and GLIS2 TG with FPC-regulated, KD-affected genes. To evaluate the crosstalk between hepatocytes with loss of ELF3 or GLIS2 and HSC, a set of NASH-induced hepatokines significantly modulated by *Elf3* and/or *Glis2* KD ($P_{adj} < 0.1$, FPC miRNA-NC vs FPC miRNA-KD) was identified. The target gene set of interest in HSC was defined as significantly induced in HSC by CCl_4 treatment (as determined above), significantly induced by FPC feeding ($P_{adj} < 0.1$, Control miRNA-NC vs FPC miRNA-NC) and significantly repressed by *Elf3* and/or *Glis2* KD ($P_{adj} < 0.1$, FPC miRNA-NC vs FPC miRNA-KD). NicheNet analyses was applied to calculate the ligand-target gene regulatory potential scores for target genes belonging to the indicated gene set of interest that were among the 2000 most strongly predicted targets of at least one of the top ligands.

Analyses of public datasets

Processed microarray and RNA-seq data was obtained from the NCBI GEO database and microarray data sets was analyzed using GEO2R. All accession numbers for the public sequencing datasets are listed in the key resources table. Raw RNA-sequencing files from Bama minipigs fed with control diet or with a high-fat, high-sucrose diet (Xia et al., 2014) were mapped to the Ss10 genome using STAR with default parameters. HOMER's analyzeRepeats.pl was used to quantify expression in annotated genes and DESeq2 was used to determine log2FC. Human clinical data for patient group definitions and correlation analyses was obtained from GEO2R. For correlation analyses of the data in GSE49541, individuals belonging to groups of mild and advanced fibrosis were assigned a score of 0.5 and 3.5, respectively. Lists of genes associated with broad H3K4me3 domains encompassing the transcriptional start site in mouse livers specific to the liver (HEP) or in ubiquitously (UBQ) broad H3K4me3 domains was obtained from (Dubois et al., 2020) and these were used to define a set of hepatocyte-selective identity genes by comparing with the RNA-seq data from HEP-INTACT mice. Processed RNA-seq data of hepatocytes isolated from control mice and the 3,5-diethoxycarbonyl-1,4-dihydrocollidine (DDC)-treated liver injury model (Merrell et al., 2021) were used to evaluate the expression of NASH-regulated genes in control hepatocytes as well as DDC-injured (YFP+/EPCAM- cells) and DCC-reprogrammed (YFP+/EPCAM+) hepatocytes. Lists of regulated proteins in

Please cite this article in press as: Loft et al., Liver-fibrosis-activated transcriptional networks govern hepatocyte reprogramming and intra-hepatic communication, Cell Metabolism (2021), https://doi.org/10.1016/j.cmet.2021.06.005

control versus NASH mice was downloaded from (Xiong et al., 2019b) and were used to investigate the overlap with proteins encoded by hepatocyte identity genes. Processed proteomics data of liver biopsies obtained from individuals diagnosed with alcoholic steatohepatitis spanning the full range of fibrosis grades (F0 to F4) was obtained from (Niu et al., 2020) and was used to select proteins that were significantly regulated during fibrosis development. This protein list was merged with proteins predicted to be expressed in hepatocytes (based on the HEP-INTACT RNA-seq data) and the enrichment of proteins encoded by hepatocyte identity genes among proteins with higher or lower mean intensity in both the F4 vs F0 stage and F3 vs F0 stage was evaluated.

QUANTIFICATION AND STATISTICAL ANALYSIS

Statistical analyses were performed using Prism (version 9.1.0, Graphpad) or the statical software R (3.6.2). Further details (including statistical tests and definitions of centers and dispersion) are available in the figure legends. Unless stated otherwise, all bar plots show data as mean ± standard error mean (SEM) and box plots depict the first and third quartiles as the lower and upper bounds of the box, with a thicker band inside the box showing the median value. Whiskers in boxplot indicate either min-to-max with all data-point shown or 1.5x the interquartile range (IQR) as indicated. Normal distribution of experimental groups at the 0.05 level was evaluated using the D'Agostino-Pearson omnibus normality test and statistically significant outliers was identified using the ROUT method (Q = 1 %). Statistical difference between one comparison of two experimental conditions was determined using a two-tailed, unpaired t-test or a nonparametric, two-sided Wilcoxon–Mann–Whitney test, as indicated. P values obtained from multiple t-tests were corrected using the two-stage linear step-up procedure of Benjamini, Krieger and Yekutieli, using an FDR cutoff < 5%. A non-parametric, one-sample Wilcoxon signed rank test was used to determine if the median of a sample was different from 0. One-way analysis of variance (ANOVA) was used to determine if there were statistically significant differences between three or more independent groups if the data was normally distributed, or alternatively a Kruskal–Wallis one-way analysis was applied if the data was not normally distributed. A two-way ANOVA was used to determine significant differences between groups that had been split on two independent variables. In all these cases, the criterion for statistical significance was $p < 0.05$. In post-hoc analyses, p values were corrected for multiple testing according to Tukey, Dunnett, Sidak or by controlling the FDR via the two-stage linear step-up method, as indicated. To investigate the significance of overlap between gene groups, the Fisher's Exact Test was used for determination of the p values, the odds ratio and the 95% confidence interval. When using GO-seq for functional enrichment analyses, the obtained p values were corrected for multiple testing using the Benjamini–Hochberg method. No power calculations were used to predetermine sample sizes.